

Using cosmic-ray hodoscope data to validate the misalignment model of small-strip thin gap chambers for the ATLAS new small wheels

Lia Formenti

Department of Physics
McGill University, Montreal
August, 2021

A thesis submitted to
McGill University
in partial fulfillment of the
requirements of the degree of
Master of Science

© Lia Formenti 2021

Table of Contents

1	Introduction	1
2	The LHC and ATLAS experiment	3
2.1	Physics Motivation	3
2.2	The Large Hadron Collider	3
2.3	The ATLAS experiment	4
3	The New Small Wheels	11
3.1	Motivation for the New Small Wheels (NSWs)	11
3.2	Design of the NSWs	12
3.3	Small-strip thin gap chambers	15
3.4	sTGC Quadruplet Construction	18
3.5	NSW alignment	19
4	Using cosmic muons to measure relative strip position offsets	22
4.1	Collecting cosmic muon data	22
4.2	Rebuilding cosmic muon tracks for characterization	24
4.3	Measuring local offsets in strip pattern using cosmics data	26
4.4	Visualizing relative misalignments between layers	30
4.5	Systematic uncertainty in cosmic residual means	30
5	Using x-rays to measure relative strip position offsets	33

6 Comparing cosmic muon and x-ray relative strip position offsets	37
6.1 Method for comparing x-ray and cosmics data	37
6.2 Assessing correlation	38
6.3 Limitations	41
7 Outlook	42
7.1 Next steps	42
7.2 Importance in context	43
References	44
APPENDICES	50
A Cluster position uncertainty	51
A.1 Cluster definition	51
A.2 Effect of fit algorithm on cluster mean	51
A.3 Effect of uncertainty in cluster mean on track residuals	52
B Analysis statistics	53
C Analysis systematics	55
C.1 Residual distribution fit function	55
C.2 Cosmic muon data collection voltage	56
C.3 Cluster fit algorithm	58
C.4 Differential non-linearity	59
D Printable plots	63

Abstract

ATLAS is a multi-purpose particle detector system designed to capture the outcome of proton-proton collisions at the Large Hadron Collider (LHC) at CERN. The innermost end-caps of the ATLAS muon spectrometer consist of two wheels of muon detectors that must be replaced to improve the angular resolution of tracks for precision muon momentum reconstruction in the next phase of LHC operation. The New Small Wheels (NSWs) will be covered with two detector types that must trigger on and track outgoing particles - one type is small-strip thin gap chambers (sTGCs). Canada is responsible for one quarter of the required sTGCs. At McGill University, modules with four layers of sTGCs (called quadruplets) are characterized using a cosmic ray hodoscope before being sent to CERN for further testing and integration into the wheels. Quadruplets must be able to reconstruct particle tracks with 1 mrad angular resolution. Misalignments between sTGC layers must be corrected for to achieve this goal. The charge profile left by an x-ray gun and coordinate measuring machine (CMM) measurements of quadruplet layers are being used to define these parameters. Work on using cosmic ray data to validate misalignment parameters derived using the above-mentioned methods will be presented.

Résumé

C'est le résumé.

Ad eros odio amet et nisl in nostrud consequat iusto eum suscipit autem vero enim dolore exerci, ut. Esse ex, magna in facilisis duis amet feugait augue accumsan zzril. Lobortis aliquip dignissim at, in molestie nibh, vulputate feugait nibh luptatum ea delenit nostrud dolore minim veniam odio. Euismod delenit nulla accumsan eum vero ullamcorper eum ad velit veniam. Quis, exerci ea feugiat nulla molestie, veniam nonummy nulla. Elit tincidunt, consectetur dolore nulla ipsum commodo, ut, at qui blandit suscipit accumsan feugiat vel praesent.

Dolor zzril wisi quis consequat in autem praesent dignissim, sit vel aliquam at te, vero. Duis molestie consequat eros tation facilisi diam dolor augue. Dolore dolor in facilisis et facilisi et adipiscing suscipit eu iusto praesent enim, euismod consectetur feugait duis vulputate.

Acknowledgements

Something along the lines of . . . I would like to thank all the little people who made this thesis possible.

Contribution of authors

Something along the lines of . . . I hereby declare that I am the sole author of this thesis. This is a true copy of the thesis, including any required final revisions, as accepted by my examiners.

Chapter 1

Introduction

The High-Luminosity Large Hadron Collider (HL-LHC) project [1] was approved to combat the plateau in statistical gain of recording particle collisions at the LHC [2] at CERN. Being the most energetic particle accelerator, the LHC still offers unique physics opportunities for studying the Higgs and electroweak sectors of the standard model[3]; if the study at the energy frontier is to continue, the LHC must go on. The HL-LHC upgrade aims to increase the luminosity of the LHC by up to a factor of 7 in the next 10 years, which ultimately increases the number of meaningful collisions. Naturally, various sub-systems of the experiments used to capture the outcomes of the collisions will require upgrades to handle higher collision rates and background radiation rates than they were designed for.

The ATLAS experiment [4] is one of the LHC’s general-purpose particle detector arrays, positioned around one of the collision points of the LHC. It detects the products of LHC collisions. During the 2019-2022 Long Shutdown of the LHC, the most complex upgrade of the ATLAS experiment is the replacement of the small wheels of the muon spectrometer with the so-called New Small Wheels (NSWs) [5]. The NSW upgrade addresses both the expected decrease in hit efficiency in the precision tracking detectors of the current small wheel expected and the high fake trigger rate of the muon spectrometer. Two different detector technologies will be installed, stacked on the NSW frame: micromegas (MMs) and small-strip thin gap chambers (sTGCs). MMs are optimized for precision tracking while sTGCs are optimized for rapid triggering, although each will provide complete coverage and redundancy over the area of the NSW. Canada was responsible for providing 1/4 of the required sTGCs.

To reduce the fake trigger rate, the NSW will provide better track angular resolution to the ATLAS trigger system to reject tracks that do not originate from the collision [5]. sTGCs provide 100 μm position resolution per detector plane [6], and are stacked in four (called an

sTGC quadruplet) to provide 1 mrad angular resolution on tracks [5, 7]. To be fast enough to provide this information to the trigger, they were designed with the smallest number of readout electrodes [5]. sTGCs are gas ionization chambers where a thin volume of gas is held between two cathode boards. One board is segmented into pad electrodes (of varying areas around 300 cm^2) and one is segmented into strip electrodes of 3.2 mm pitch. The signals picked up by the pads due to a passing charged particle are used to select which strip electrodes to readout. The position of the particle track in the precision coordinate can then be reconstructed from the strip signals to provide the track angle to the trigger fast enough for the trigger to decide if the particle came from the interaction or not [5].

Precise position resolution is gained without accurate positioning of readout electrodes in ATLAS. The ATLAS alignment system is able to position the surface of three sTGC or MM quadruplets traversable by a muon track with respect to one another within 40 μm . The internal geometry of the detectors must be controlled or corrected for to within the chambers' position resolution [5]. Corrections to the position of strip electrodes in sTGC quadruplets are in their final stages. The corrections are done with characterization data collected throughout the construction process. At the cathode board level, strip electrode positions are digitized with a coordinate measuring machine (CMM) [8]. At the quadruplet level, sTGC quadruplets are characterized with cosmic rays and with an x-ray gun at positions that will be tracked by the alignment system. Cosmic muon data can be used to measure relative strip position offsets in a chosen area with respect to other layers, which is useful for quadruplet characterization but does not allow the strips to be positioned in the absolute ATLAS alignment system. The x-ray method [9] is able to measure offsets of the strip pattern near the x-ray gun in a coordinate system accessible to the alignment system; however, it is limited to a handful of positions on the surface of the quadruplet and should be validated by an independent method. In this work, cosmic muon data is used to measure relative strip offsets, the x-ray method is validated with cosmic muon data, and how this work fits into the overall alignment scheme is presented.

Chapters 2 and 3 give more details on ATLAS, the LHC, the NSW, and sTGCs required to understand the context of this work. In chapter 4, the cosmic ray testing procedure and how the position of the strips can be probed with cosmic data is presented. Chapter 5 introduces the x-ray method, and in chapter 6, the x-ray offsets are validated with cosmic muon data. The thesis concludes with a summary and outlook in chapter 7.

Chapter 2

The LHC and ATLAS experiment

The LHC and ATLAS experiment are introduced here to provide context for the New Small Wheel upgrade. **Adjust this based on new physics motivation section**

2.1 Physics Motivation

Gotta write this

2.2 The Large Hadron Collider

The LHC is an accelerator 27 km in circumference and located \sim 100 m underground at CERN near Geneva, Switzerland [2]. It has two beam pipes that counter-circulate bunches of protons¹ before colliding the bunches in the center of one of four major experiments, such as the ATLAS experiment (discussed in section 2.3). There, the partons interact and many physics processes can occur. The LHC enables physicists to study particle physics at the energy frontier. In the previous run of the LHC (run-2), protons were collided with a center of mass energy of 13 TeV.

The number of proton-proton interactions generated by the LHC directly affects the statistics available to make fundamental measurements of cross sections, event rates, etc. Predicting the number of proton-proton interactions requires defining a metric called luminosity [10].

¹the LHC also accelerates lead ions, but this paper is written in the context of proton-proton collisions

It is the number of particles an accelerator can send through a given area per unit time. It is calculated from the measurable quantities in equation 2.1.

$$\mathcal{L} = \frac{f N_1 N_2}{4\pi\sigma_x\sigma_y} \quad (2.1)$$

In equation 2.1, f is the frequency of the bunch crossings (25 ns), N_1 and N_2 are the number of protons in each bunch ($\sim 10^{11}$ protons / bunch), and σ_x and σ_y are the RMS of the spatial distributions of the bunch. Therefore, luminosity is a property of the accelerator and its operating parameters. The design luminosity of the LHC was $10^{34} \text{ cm}^{-2}\text{s}^{-1}$. The units of luminosity are an inverse area; multiplying the luminosity by the cross section of a given process gives the expected rate for that process.

Integrating the *instantaneous* luminosity (equation 2.1) over a period of data collection gives the integrated luminosity,

$$L = \int \mathcal{L}(t) dt \quad (2.2)$$

which is related to the total number of interactions. In this way, the luminosity is the link between the accelerator and the statistical power of measurements to be made with the data collected.

So far, the LHC provided an integrated luminosity of 28.26 fb^{-1} in run-1 [11] and 156 fb^{-1} in run-2 [12], as shown in figure 2.1. The HL-LHC upgrade [1] was accepted because without increasing the luminosity of the LHC tenfold, running the accelerator will not provide significant statistical gain on measurements. Also, some systems will need repair and replacement to operate past ~ 2020 . The energy accessible at the LHC offers irreplaceable ability to study Higgs- and electroweak-sector physics [3], so the European Strategy for Particle Physics made it a priority “to fully exploit the physics potential of the LHC” with “a major luminosity upgrade” [13]. The goal is for the HL-LHC to provide an integrated luminosity of 3000 fb^{-1} in the 12 years following the upgrade. The luminosity actually achieved will depend on a combination of technological advances and upgrades in progress that affect the factors contributing to luminosity defined in equation 2.1 [1].

2.3 The ATLAS experiment

The ATLAS experiment [4] was designed to support all the physics goals of the LHC. It is 44 m long and 25 m in diameter, and weighs 7000 tones. It is an array of particle detector



Figure 2.1: LHC/HL-LHC plan [14]. The integrated luminosity collected and projected for each run of the LHC is shown in red below the timeline and the center of mass energy of the collisions is shown in red above the timeline. The top blue arrow labels the run number. “LS” stands for “long shutdown” and indicates periods where the accelerator is not operating. During the shutdowns, upgrades to the LHC and the experiments are being installed. This timeline was last updated in January, 2021, and reflects changes in the schedule due to the ongoing pandemic.

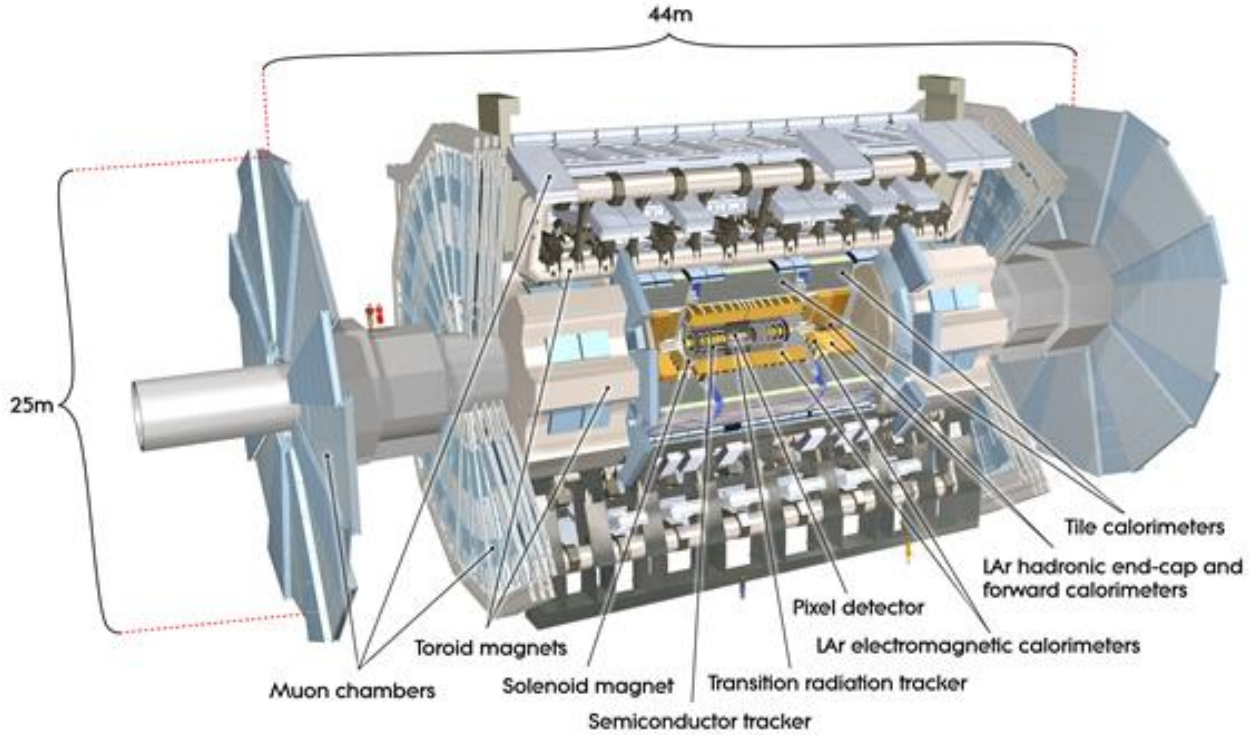


Figure 2.2: Diagram of the ATLAS experiment, with the various detector subsystems labelled. Figure from [4], which also contains more details about the ATLAS experiment.

subsystems arranged concentrically around the beam pipe and centered around one of the LHC's interaction points (a place where the beams collide), as shown in figure 2.2. ATLAS is cylindrical because it aims to provide 4π coverage around the interaction point. It is helpful to separate the subsystems of ATLAS into the so-called “barrel” and “endcap” or “forward” regions.

For analysis, ATLAS is typically described in spherical coordinates. The azimuthal angle ϕ is measured around the beampipe and the polar angle θ is measured from the beam pipe. A more useful coordinate than θ is the pseudo-rapidity, $\eta = -\ln \tan(\theta/2)$, because it approaches the rapidity of a particle when its momentum is much greater than its mass and differences in rapidity are approximately invariant to a Lorentz boost parallel to the beam. The range of η is 0 (perpendicular to the beam) to $\pm\infty$ (parallel to the beam, or the z-direction). Typically, η is the physically interesting coordinate because the ϕ coordinate follows the cylindrical symmetry of the beam.

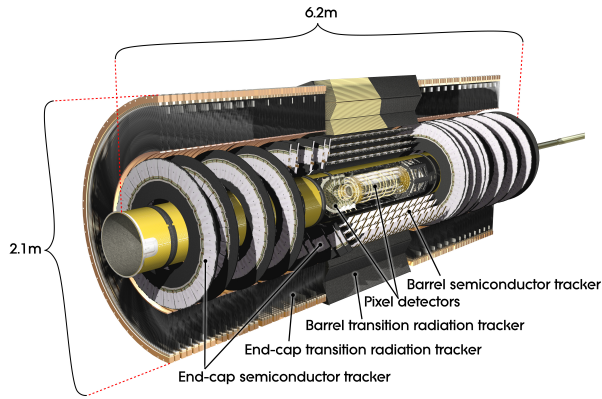


Figure 2.3: Diagram of the ATLAS experiment’s inner detector, with the different segments and the technology used labelled. Figure from [4].

It is not actually the proton bunches that collide and generate physics processes, but their constituent partons. Since the partons may carry an unknown fraction of the momentum, ATLAS analyses are based on the sum of the transverse momentum (p_T) and energy of outgoing particle being approximately zero (transverse meaning perpendicular to the beam). **The goal of ATLAS is to reconstruct the transverse momentum of each collision product to understand what happened in each collision. - δ Do I have this right?** A brief overview of the sub-systems of ATLAS is given, starting from the system closest to the beam and moving outwards. Each sub-system is responsible for a different group of collision products.

The inner detector

The inner detector [15, 16] (figure 2.3) is for precision tracking, vertex measurements and electron identification. A 2 T solenoid with field parallel to the beam bends the track of outgoing particles to make momentum measurements possible. The innermost part is made of high-resolution semiconductor pixel and strip detectors for precision tracking while the outermost part are straw-tubes that generate and detect transition radiation for electron identification.

Calorimetry system

Electromagnetic and hadronic sampling calorimeter units are used to record the energy of electrons, photons, jets and missing transverse energy (from neutrinos, for example). A combination of liquid-argon (LAr) electromagnetic and hadronic calorimeters [17] and tile-scintillator hadronic calorimeters [18] cover the rapidity range $|\eta| < 4.9$, as shown in

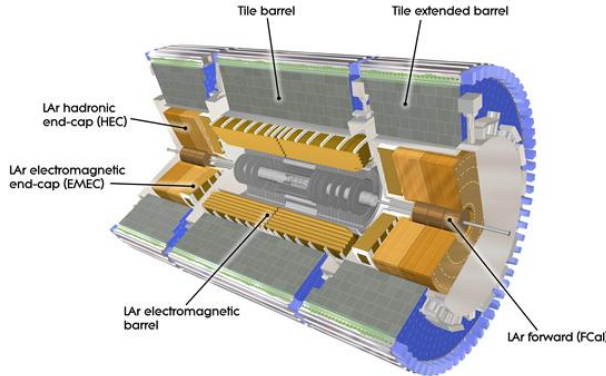


Figure 2.4: Diagram of the ATLAS calorimeter system, with the different segments and the technology used labelled. Figure from [4].

figure 2.4.

The calorimeters cause incoming charged particles to shower and deposit their energy in the sensitive volume. Only muons and neutrinos are known to pass the calorimeters to the muon spectrometer. Particles other than those mentioned would have decayed in the inner detector before reaching the calorimeter.

Trigger system

It would be impossible to record all the data from bunch crossings every 25 ns, corresponding to a rate of ~ 40 MHz, so ATLAS has a multi-level trigger system to select events of interest for permanent storage. The Level-1 (L1) hardware trigger [19] uses partial-granularity information from the muon spectrometer and calorimeter to trigger on high p_T muons, electrons, jets, high missing transverse energy, and τ decaying to hadrons. The maximum L1 trigger rate ATLAS can accommodate is 100 kHz with a latency of 2.5 μ s.

The L1 trigger is used to define regions of interest that are fed into the software high level trigger (HLT), in which the full granularity of the muon spectrometer and calorimeter are used with information from the inner detector to reduce the trigger rate to 1 kHz. Events that pass the L1 and HLT trigger are recorded for use in offline analysis [20].

The ATLAS trigger system is described in the references above but the trigger rates quoted here are after the upgrades implemented for run-2, described in [21].

Muon spectrometer

Magnetic deflection by superconducting air-core toroid magnets is used to measure muon

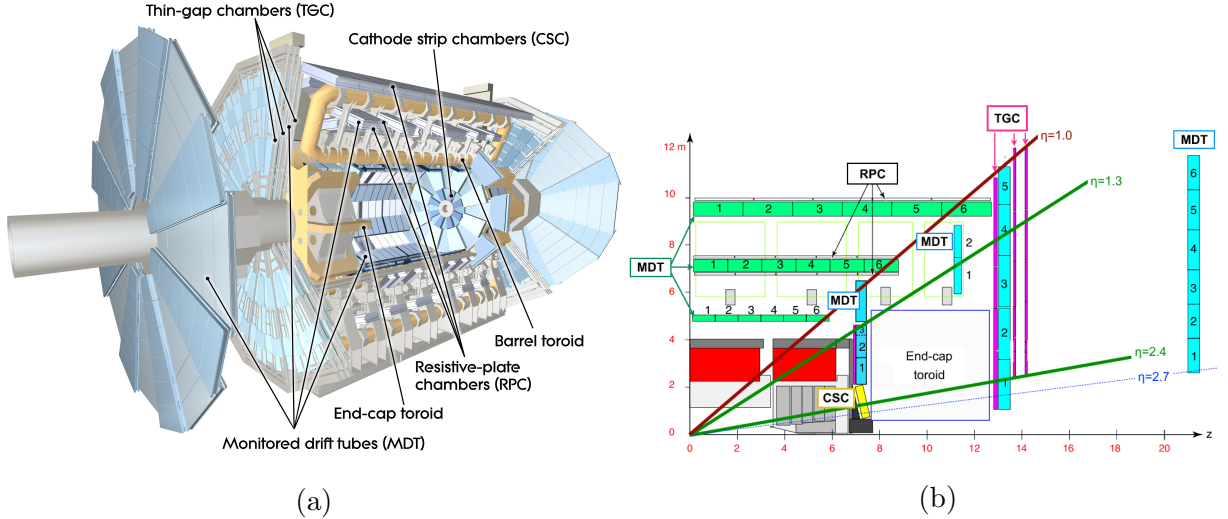


Figure 2.5: (a) The ATLAS muon spectrometer [4]. (b) A quarter-cut of ATLAS, with the interaction point in the bottom left corner. The small wheel is just left of the end cap toroid, the big wheel is to its right, and the outer wheel is the rightmost structure [23]

momentum and energy. In the barrel of ATLAS, eight coils bent into “racetracks” are arranged around the beampipe provide the magentic field. In the forward region, two end-cap toroids each with eight smaller racetrack-shaped coils arranged symmetrically around the beampipe are inserted in the ends of the barrel toroid [22]. Figure 2.5 shows the toroid magnets and the different parts of the ATLAS muon spectrometer.

The muon spectrometer [24] is separated into detectors used for precision offline tracking and for triggering. Three layers of monitored drift tubes (MDTs) or cathode strip chambers (CSCs) are used for tracking. The position of the muon track in each of the three layers allows reconstruction of the track sagitta and hence momentum. For the design momentum resolution of $\Delta p_T/p_T < 1 \times 10^{-4} p / \text{GeV}$ for $p_T < 300 \text{ GeV}$ and a few percent for lower p_T muons, the MDTs and CSCs required position resolution of $50 \mu\text{m}$ each. Accordingly, an optical alignment system was designed to monitor and correct for chamber positions [24, 25].

Resistive plate chambers (RPCs) are used for triggering in the barrel and thin-gap chambers (TGCs) are used for triggering in the endcaps. The positions of each type of chamber are sketched in figure 2.5b. Often, the endcap muon spectrometer is separated into three wheels – the small wheel (SW), big wheel, and outer wheel – ordered by proximity to the interaction point. In run-1, low (high) p_T muons were triggered on at L1 if two (three) of the RPCs or TGCs layers around the big wheel fired in coincidence, for the barrel and endcaps respectively [19]. After run-1 it was discovered that up to 90% of the triggers in the endcap

were fake, caused by background particles generated in the material between the small wheel and the big wheel [5]. To reduce the fake rate in run-2, the TGCs on the inside of the small wheel also had to register a hit. The added condition reduced the trigger rate by 50% in the range $1.3 < |\eta| < 1.9$ [21]. The effectiveness of the solution was limited since the $|\eta|$ -range of the small wheel TGCs was limited to $1.0 < |\eta| < 1.9$ and the position resolution of the small wheel TGCs is coarse [5].

Chapter 3

The New Small Wheels

3.1 Motivation for the New Small Wheels (NSWs)

The hit rate of all detector systems will increase with the HL-LHC not only because of the increase in luminosity, but also because the background radiation rate increases linearly with luminosity. The combined rate presents problems for both the tracking and triggering capabilities of the muon spectrometer [5].

In term of tracking, the efficiency of the MDTs decreases by 35% (mostly due to long dead-times) already when exposed to the maximum hit rate at the current luminosity, 300 kHz. At the threefold increase in luminosity predicted for run-3, most of the small wheel will be subjected to a hit rate well above 300 kHz and it will begin missing hits. Losing hits in the small wheel will reduce the high p_T muon momentum resolution. The decrease in resolution will affect the ability to search for, for example, high mass Z' , W' and pseudo-scalar Higgs [5].

Already, the forward muon trigger system copes with a very high fake rate, even when including TGC data from the small wheel in the trigger as in run-2. At the luminosity expected in run 3, 60 kHz of the maximum 100 kHz of the L1 trigger would be taken by the endcap muon spectrometer. A possible solution would be to raise the minimum p_T threshold from 20 GeV to 40 GeV, but the ability to study several physics processes of interest depend on low p_T muons [5]

The NSW will solve both these problems. It will be covered with precision tracking chambers suitable for the expected hit rates and triggering chambers capable of 1 mrad angular resolution. The idea behind the triggering chambers is to match the small wheel track segment with the track segment from the big wheel to discard tracks not originating from the inter-

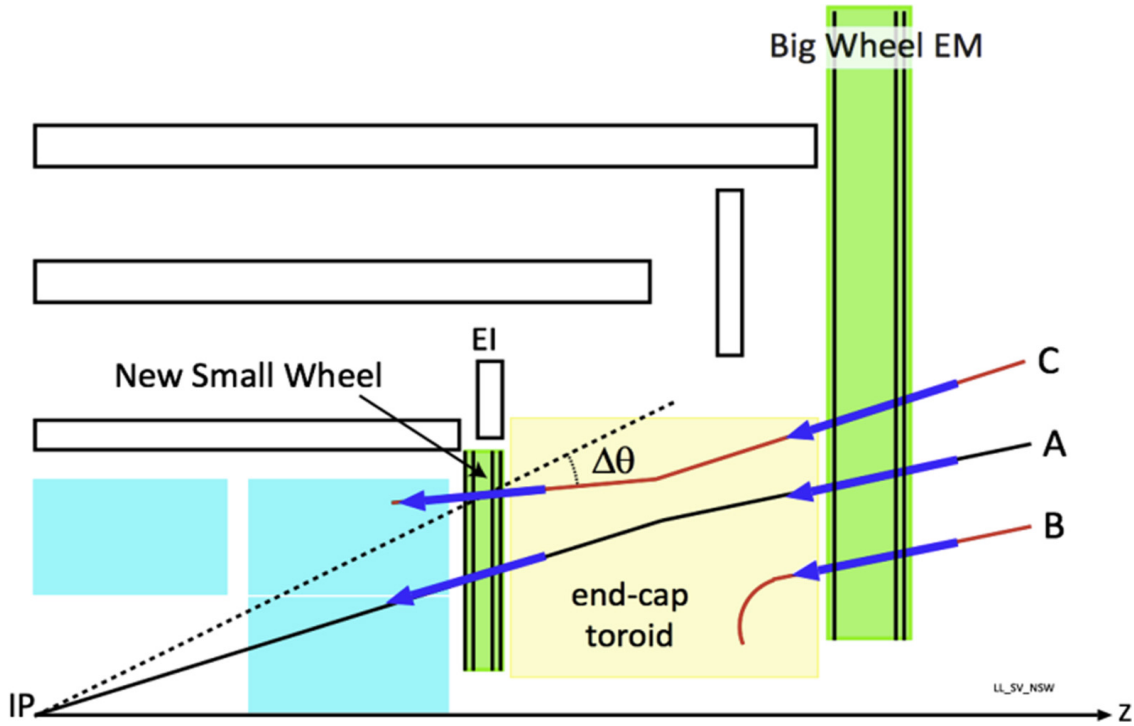


Figure 3.1: A schematic of a quarter cross section of the ATLAS detector, with the collision/interaction point (IP) in the bottom left corner. Three possible tracks are labelled. Ideally, track A would be triggered upon while track B and C discarded. With the small wheel, all three tracks would be recorded. With the NSW, only track A would be recorded [5].

action point. Figure 3.1 illustrates this point: the run-1 trigger system would have triggered on all three tracks, while with the NSW the trigger system would only trigger on track A [5].

3.2 Design of the NSWs

The NSWs are covered with two detector technologies: micromegas (MM) and small-strip thin gap chambers (sTGCs). MMs are the primary tracking detectors and sTGCs are the primary triggering detectors, but for redundancy sake both are designed to do either. As such, both sets of detectors are to have position resolution better than $\sim 100 \mu\text{m}$ per plane. Four chambers of each type are glued together to create quadruplet modules. Quadruplets of different sizes are assembled into wedges. Two sTGC wedges and two MM wedges are layered to create sectors (with the sTGC wedges on the outside) [5]. Different stages of the

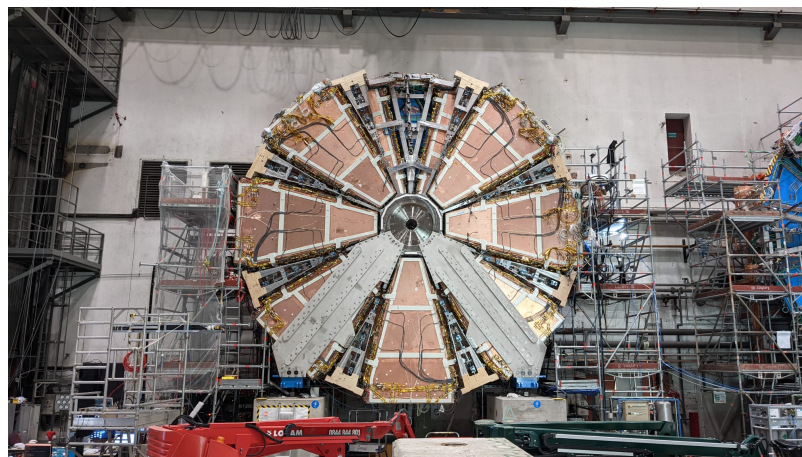
constrcution process are shown in figure 3.2.



(a) An sTGC quadruplet module. The left image highlights the trapezoidal shape. The right image shows the short edge corner. The four sTGC layers and each layer's gas inlet are visible. The gas outlets and high voltage cables are at the long edge in the back of the photo. The green printed circuit board along the sides are the adaptor boards where the front end electronics are attached.



(b) Left: An sTGC wedge. The white frame outlines the individual quadruplet modules. Right: A completed sector, with two sTGC wedges on the outside and two MM wedges on the inside.



(c) The new small wheel. All sectors except one large sector at the top are installed, revealing two of the smaller sectors that are normally hidden under the large sectors and support bars. The NSWs are 10 m in diameter.

Figure 3.2: Images breaking down some of the construction units of the NSWs.

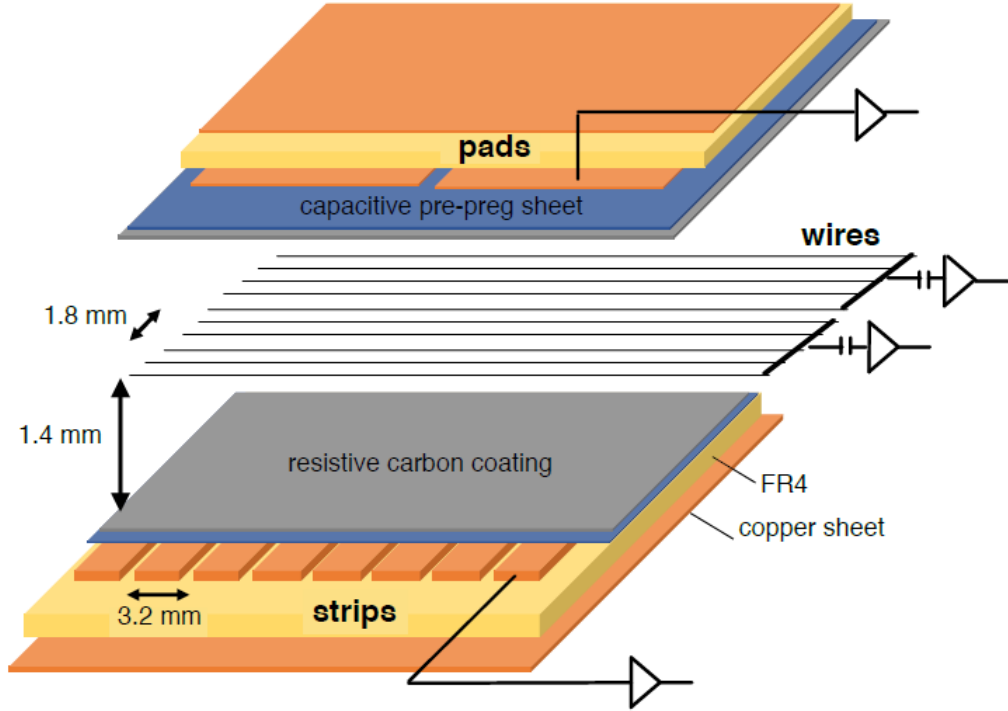


Figure 3.3: Internal structure of an sTGC, zoomed into the area under approximately 1 pad. High voltage is applied to wires suspended in the gas volume to create an electric field. A passing muon causes an ionization avalanche that is picked up by the wire, strip and pad electrodes [9].

3.3 Small-strip thin gap chambers

sTGCs are gas ionization chambers operated with a CO₂:n-pentane ratio of 55:45. Gold-plated tungsten wires, 50 µm in diameter and with 1.8 mm pitch, are suspended between two cathode planes made of FR-4, each 1.4 mm away (see figure 3.3). One cathode board is segmented into pads of varying area (around 300 cm² each), and the other segmented into strips of 3.2 mm pitch, perpendicular to the wires. High voltage is applied to the wires and the cathode planes are grounded [5, 7]. When a muon passes through, the gas is ionized and the electric field in the gas gap causes an ionization avalanche [26]. The motion of the ions and electrons are picked up on the nearby wire, strip and pad electrodes. The resistivity of the carbon coating and capacitance of the pre-preg sheet tune the spread of the charge

distribution [27] and the speed of the response [28] to optimize the rate capability. The hatching of the strips and wires establishes a coordinate system from which to extract the coordinate of the muon as it passes through the layer [5].

A 3-out-of-4 coincidence in the pad electrodes of a quadruplet will define a region of interest where the strip and wire electrodes should be readout. Then, a track segment with the required angular resolution can be constructed quickly enough to be provided as input to the hardware trigger [5]. The pad-triggering scheme greatly reduces the number of electrodes that require readout to provide the design track angular resolution of 1 mrad. For the next run of ATLAS (run-3), the L1 trigger will pass if the track segment from the small wheel matches a region of interest defined by the TGCs of the big wheel [29, 5]. The increased angular resolution and η coverage of the quadruplets will be an improvement in the triggering scheme over the current small wheel TGCs [5]. After the phase-II upgrade of the trigger and data acquisition system scheduled for \sim 2025, which includes upgrades to the big wheel’s angular resolution, there will only be a trigger if the combined track points back to the interaction point, increasing the muon p_T resolution [5, 30].

Signal is readout from groups of successive wires, so the position resolution in the direction perpendicular to the wires is 10 mm. The resolution in this direction is sufficient since it will give the symmetric azimuthal coordinate in ATLAS. Good resolution on the η coordinate, perpendicular to the strips, is important [5]. The average single chamber position resolution in the strip coordinate was 45 μm for perpendicular muon tracks as measured in a test beam [6] — well within design specifications. When four sTGCs are glued together into a quadruplet the design angular resolution of 1 mrad in the strip coordinate is achievable [5, 7].

Therefore, sTGCs are able to meet the precision tracking and triggering goals they were designed for. To ensure they can deliver once installed in ATLAS, knowing the position of the strips to within their position resolution in the ATLAS coordinate system is necessary. The NSW alignment system, detailed in section 3.5 monitors the position of alignment platforms installed on the surface of the wedges. The alignment platforms are installed with respect to an external reference on the sTGCs: two brass inserts on each strip layer on one of the angled sides of each quadruplet (shown in figure 3.4). So the challenge of positioning the strips in ATLAS was separated into two steps: first, position the strips with respect to the brass inserts; second use the alignment system to position the alignment platforms. The next section provides some pertinent details on the sTGC construction process, with steps that affect the position of the strips with respect to the brass inserts highlighted.



(a) Brass insert near long edge.

(b) Brass insert near short edge.

Figure 3.4: The brass inserts sticking out from the gas volumes of an sTGC quadruplet. These inserts were pressed against alignment pins when the individual sTGCs were being glued together.

3.4 sTGC Quadruplet Construction

Five countries were responsible for producing the sTGC modules of varying geometries for the NSW: Canada, Chile, China, Israel and Russia. Canada was responsible for 1/4 of the required sTGCs, of three different quadruplet geometries. The steps of the construction process in each country were similar [5]. The process followed in Canada is detailed.

TRIUMF in Vancouver, British Columbia was responsible for preparing the cathode boards. The boards were made and the electrodes etched on at a commercial laboratory, Triangle Labs, in Carson City, Nevada. Once completed they were sent to TRIUMF to be sprayed with graphite and otherwise prepared [8]. The boards are commercial multilayer printed circuit boards, but the strip boards required precision machining to etch the strip pattern [5]. Triangle Labs also machined the two brass inserts into each strip board. A coordinate measuring machine (CMM) was used to digitize each strip. Four quality parameters describing non-conformities in the strip pattern of each board with respect to the brass inserts were derived from the data and the results are available on a QA/QC database. The parameters and the so-called CMM data is described in full in Carlson's thesis [8]. Due to time constraints, tolerances on the non-conformities in the etched strip pattern with respect to the brass inserts were loosened, with the condition that the strip positions would have to be corrected for [8].

The prepared boards were sent to Carleton University in Ottawa, Ontario for construction into sTGCs and quadruplets. First, the wires were wound around the pad cathode boards using a rotating table and the wires were soldered into place. A wound pad cathode board was held by vacuum on a granite table, flat to within $20\text{ }\mu\text{m}$ and a strip cathode board glued on top to create an sTGC. Holding one sTGC flat with the vacuum, another was glued on top to create a doublet, then two doublets were glued together to create a quadruplet. When gluing sTGCs together, the brass inserts were pushed against alignment pins with the goal of keeping the strip layers aligned within tolerance. However, non-conformities in the shape of the brass inserts, non-conformities in the position of the alignment pins and shifts between strip layers while the glue cured resulted in misalignments between the brass inserts – and the strips – on successive layers. Precise alignment of the pad boards or wires with respect to the strip boards did not have to be so tightly controlled because pads do not measure the precision coordinate.

The Carleton team finished the quadruplets by installing adaptor boards on the angled sides of each layer that allow front end electronics to be attached. Completed quadruplets were sent to McGill University where they were characterized with cosmic rays. The details of cosmic ray testing are described in chapter 4. Quadruplets were then sent to CERN where they were assembled into wedges and alignment platforms installed. The alignment platforms

were installed using a jig positioned with respect to the brass inserts. Completed wedges were assembled into sectors then installed on the NSWs.

The quadruplet construction process had two steps where strip positions could be shifted off of nominal. At board-level, there could be non-conformities in the etched strip pattern with respect to the brass inserts, described by the four quality parameters [8]. At the quadruplet level, misalignments between the brass inserts and strips on different layers were introduced during the gluing. The result was that the brass inserts were not a reliable reference point and that the strips can be offset from their design position by up to hundreds of micrometers. Offsets in strip positions from nominal in Canadian quadruplets were shown to be random [8], so no one correction would suffice. The offsets must be measured and corrected for in the ATLAS offline software, **Athena**, which does the precision tracking. Understanding the work ongoing to make measurements of offsets and correct for them requires understanding the strategy of the NSW alignment system.

3.5 NSW alignment

What figures can I use to show the bars, the alignment jig, the platforms and the optical fibres?.

The idea of the NSW alignment system is presented in [5], but the details have only been presented internally so far. After the wedges are constructed, alignment platforms are installed on every sTGC quadruplet and optical fibres routed to them, as shown in figure 3.5. Light from the optical fibres will be monitored in real time by cameras (BCAMs) mounted on the alignment bars of the NSWs. The system will thus record the positions of the alignment platforms in the ATLAS coordinate system, accessible at any point during operation.

The original alignment scheme was to use the brass inserts as a reference between the alignment platforms and the individual strips, as shown in the solid arrows in figure 3.6 – this will no longer work. The position of the alignment platforms will be known thanks to the alignment system, so a different method to get the position of the individual strips with respect to the alignment platform is currently in its final stages. It uses the yet-unmentioned x-ray dataset to calculate offsets of the strip pattern of an sTGC layer in a local area (local offset) with respect to the alignment platforms by analyzing the beam profile left by an x-ray gun attached to different positions on the alignment platforms. Effectively, the reference to the brass inserts is skipped, represented as the dashed line in figure 3.6. Given that the x-ray data can only be collected at specific positions and that it is an important part of the alignment scheme, the method needs to be validated. The goal of this thesis is to validate the x-ray local offsets while exploring how cosmics data can be used to position strips and

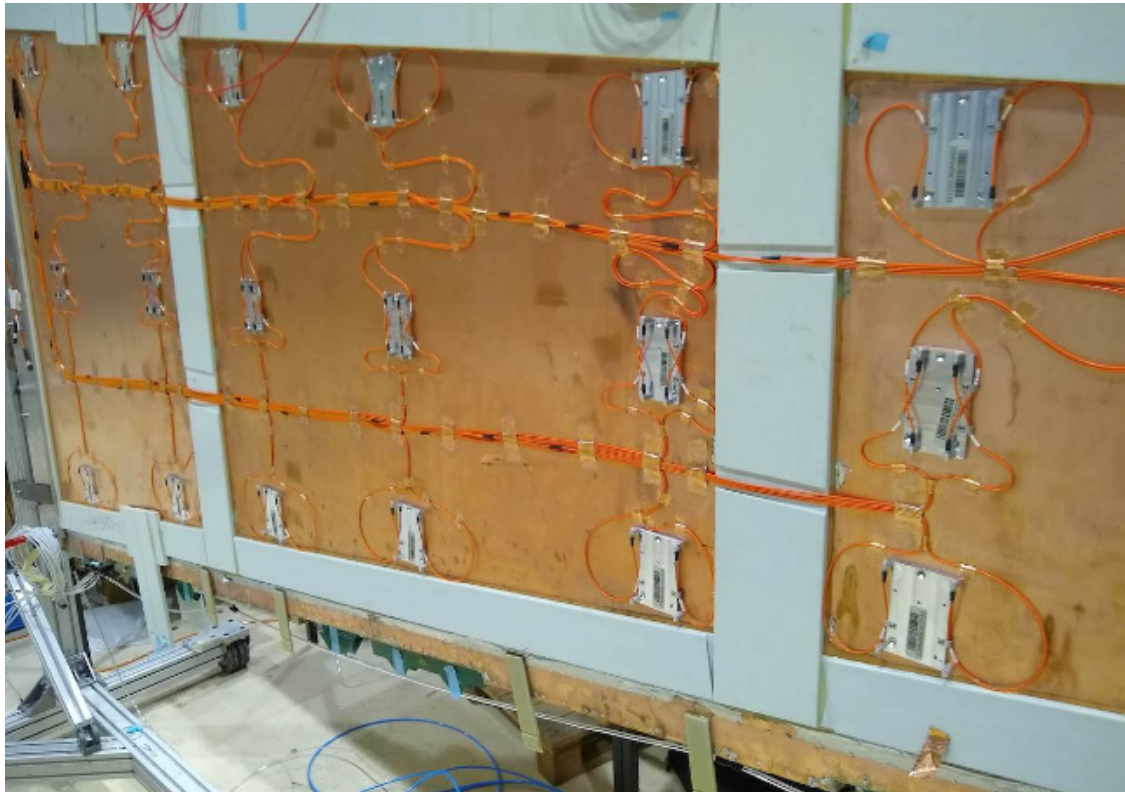


Figure 3.5: An sTGC wedge with alignment platforms (silver) installed on the quadruplet. Optical fibres (orange) are routed to the alignment platforms. Cameras on the frame of the NSW will record light from the optical fibres to position the alignment platforms in the ATLAS coordinate system.

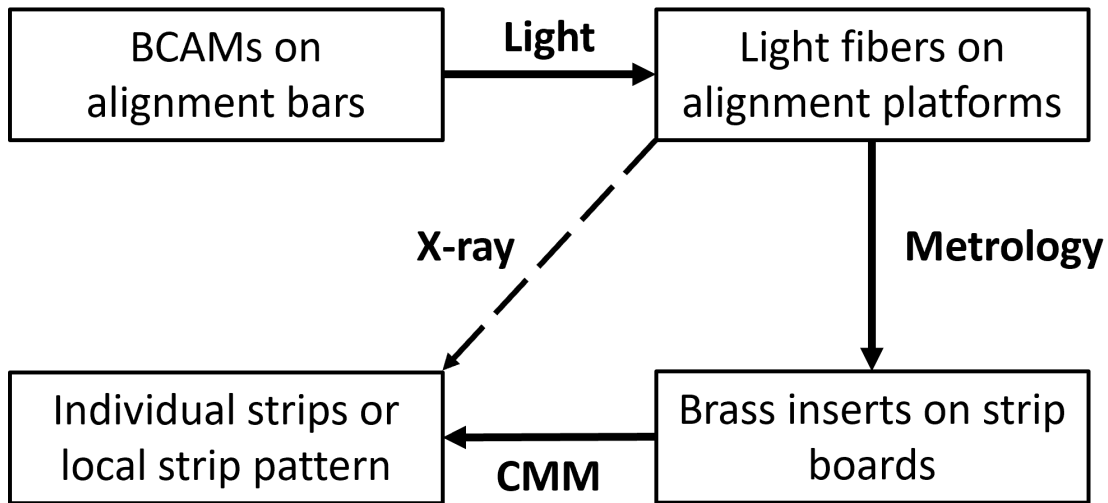


Figure 3.6: How the different elements of the sTGC alignment system relate to one another. The solid arrows denote the planned alignment scheme. The dashed arrow shows the modification being finalized now. This figure was originally designed by Dr. Benoit Lefebvre.

complement other characterization datasets being used for alignment. The next chapter explains how cosmic muon data is collected and how it can be used to study strip positions; the next chapter after explains how x-ray data is collected and how it can be used to study strip positions; and the third chapter compares the two results.

Chapter 4

Using cosmic muons to measure relative strip position offsets

In Canada, the cathode boards were prepared at TRIUMF in Vancouver; the quadruplets were constructed at Carleton University in Ottawa; and the completed quadruplets were tested and characterized with cosmic muons at McGill University in Montreal, before being sent to CERN. In this chapter pertinent details of cosmic muon testing at McGill are presented.

4.1 Collecting cosmic muon data

Cosmic muon characterization was done with a hodoscope, a complete description of which can be found in [31]. The quadruplet was placed in the center of the test bench. Above and below it was a layer of scintillator-PMT arrays, labeled in figure 4.1. When a cosmic muon passed within the acceptance of the hodoscope, at least one scintillator from the top array and at least one from the bottom array fired in coincidence and the coincident signal was used to trigger the readout of the quadruplet's electrodes. The trigger was passed to the front end boards (FEBs) attached to the adaptor boards of each layer of the quadruplet.

Each sTGC electrode was connected to a channel on an ASIC¹ on the FEB, which was set to measure and record the channel's maximum output (called peak detector output, or PDO). For each trigger, the PDO of all channels above threshold were recorded as an event and stored in a binary file. Thresholds were estimated [33] and adjusted manually in the

¹the VMM3 [32] check this in lab

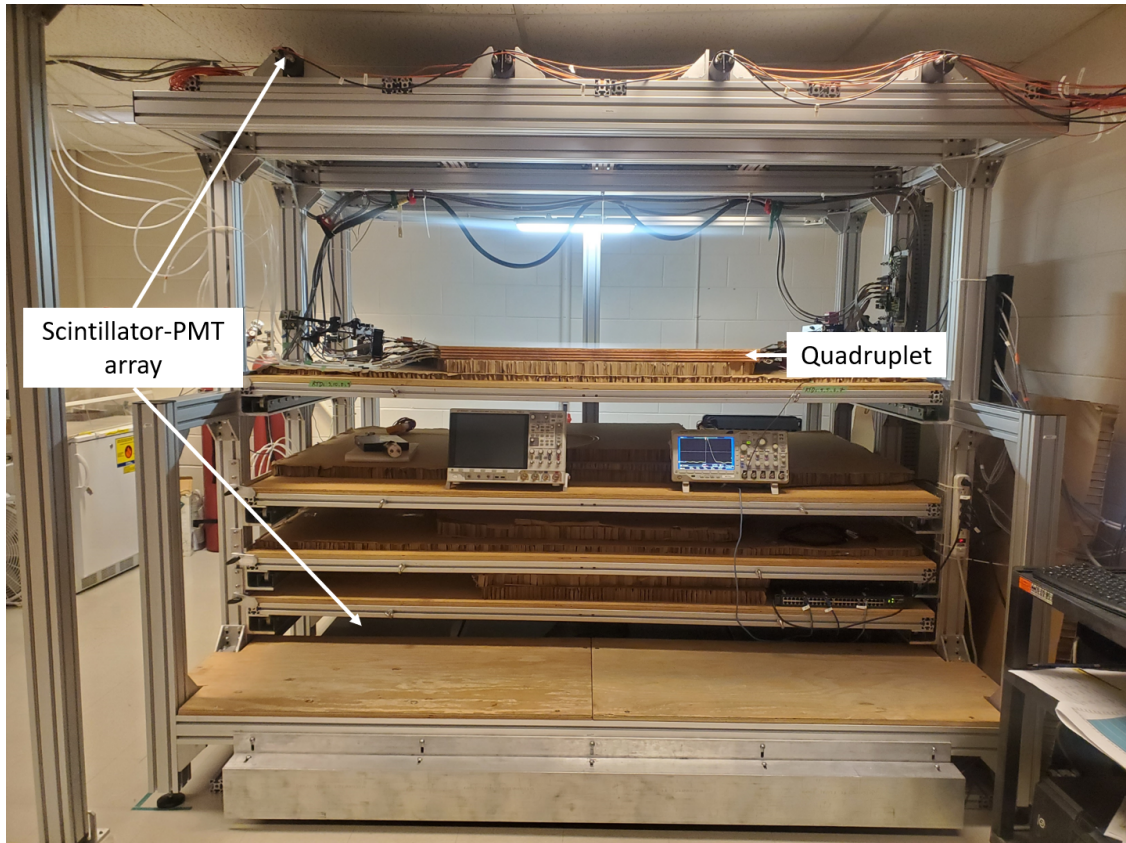


Figure 4.1: Cosmic muon hodoscope at McGill University with sTGC quadruplet in the test bench.

configuration/readout software. The binary file could be decoded into a usable ROOT tree offline.

Operating the chambers also required gas and high voltage. A pentane-CO₂ mixture was mixed and delivered to each sTGC with a gas system designed and made at McGill University. The gas system was controlled by a slow control program, also made in-laboratory [34]. High voltage was provided by CAEN boards. Cosmic muon data was collected at 2.9 kV and 3.1 kV. Although the chambers will be operated at 2.8 kV in ATLAS, the earlier version of the FEBs used at McGill had a worse signal-to-noise ratio for pads, which was compensated for operating the chambers at 3.1 kV, which increased the chambers' gain. Operating at 2.9 kV was sufficient for strip and wire signals and closer to the nominal voltage. Collecting 1 million triggers at each voltage provided enough statistics to calculate characterization metrics, which meant collecting data for just over two hours per quadruplet per voltage.

4.2 Rebuilding cosmic muon tracks for characterization

Many of the high-level characterization metrics required rebuilding muon tracks. For events passing quality cuts [35], the x- and y-coordinates of the ionization avalanche on each layer were extracted from the signal on the wires and strips respectively for each event, as is sketched in figure 4.2. In this work, x was the coordinate perpendicular to the wires and y was the coordinate perpendicular to the strips, as is drawn in figure 4.2.

The x-coordinate was taken as the center of the wire group with the maximum PDO, since the wire groups' pitch (36 mm) was larger than the typical charge spreading. Assuming that the true x-position of the hit was uniformly distributed over the width of the wire group, the uncertainty in the x-position was given by $\frac{36 \text{ mm}}{\sqrt{12}} = 10 \text{ mm}$ [36].

The y-coordinate was taken as the Gaussian mean of the PDO distribution across groups of contiguous strips. The process of grouping contiguous strips with signal above threshold² was called clustering, and the resulting group was called a cluster. Figure 4.2 sketches the clustering process and a sample cluster is shown in figure 4.3. Typically, clusters were built of 3-5 strips. The thickness of the graphite coating over the cathode boards determined how many strips picked up the ionization image charge. Larger clusters were more likely caused by δ -rays since they spread the cloud of ionization.

²Note that during cosmic ray testing, the hardware was configured to also record the PDO of strips adjacent to a strip above threshold.

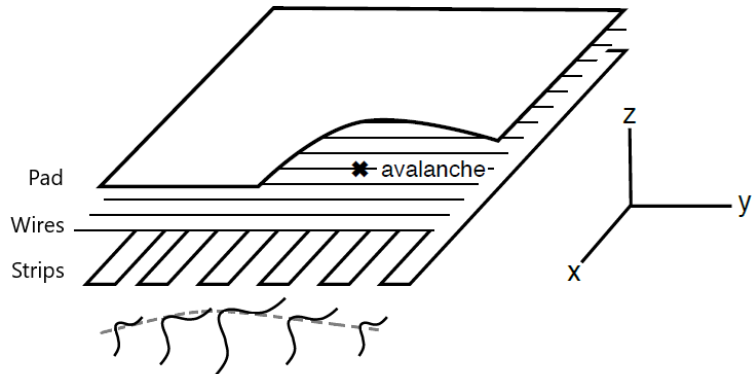


Figure 4.2: A sketch of an sTGC-like detector. The position of the avalanche could be extracted from the wires and strips that picked up the avalanche signal. The signals on individual strips are sketched. Clustering was the processs of fitting a Gaussian to the peak value of the signals on individual contiguous strips, as is done in figure 4.3. In this work, the x(y)-coordinate will always refer to the coordinate perpendicular to the wires (strips) [31, 27].

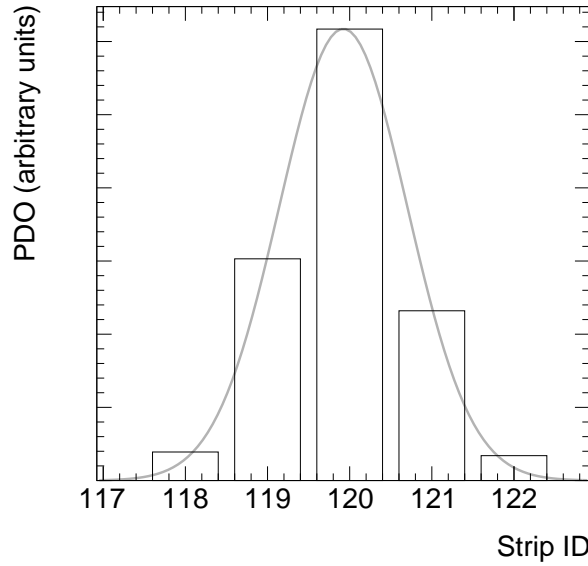


Figure 4.3: A sample cluster resulting from the current picked up on a group of strips (presumably) after the passing of a muon. The grey line is a Gaussian fit.

The uncertainty in the y-coordinate could have been taken as the fitted cluster mean's statistical uncertainty; however, after comparing the difference in cluster means for different fitting algorithms in appendix A.2, 60 μm of uncertainty was assigned.

The coordinates of the avalanches' on all layers were used to reconstruct tracks in x and y respectively. Most tracks passing quality cuts were probably cosmic muons, but of course some δ -rays and noise contributed. The tracks were then used to calculate characterization metrics like electrode efficiency and spatial resolution, the details of which are discussed in [31].

Three methods were used to characterize each quadruplet's alignment: the CMM method, cosmic ray tracing and x-ray profile reconstruction. For present purposes, the CMM method was described sufficiently in the introduction. The x-ray method is detailed in chapter 5. How cosmic ray tracing was used for alignment studies, with the goal of independently validating the x-ray method, is the main focus of this chapter and this thesis.

4.3 Measuring local offsets in strip pattern using cosmics data

Misalignments can be modeled as passive transformations. Ideally, a misalignment model would be chosen and the parameters (for example, a global offset and rotation for each layer) calculated. To understand the potential of cosmic muon data, it is useful to define a local offset. For each area of a strip layer, the local offset is the shift of the strip pattern in that area with respect to the nominal geometry. Local offsets systematically change the strip that is hit by a muon passing through the area. The `tgc_analysis/CosmicsAnalysis` software assumes the nominal geometry, so the recorded muon y-position (y) is shifted opposite to the local offset (d_{local}),

$$y = y_{nom} - d_{local}, \quad (4.1)$$

where y_{nom} is the position of the muon that would have been recorded if there was no local offset. Equation 4.1 ignores other factors that could affect the cluster position (like position resolution). The local offset is unknown and there was no external reference to measure y_{nom} . Therefore, only relative alignment parameters can be extracted.

The minimal relative coordinate system uses two reference or fixed layers [31]. The hits on the two fixed layers were used to create tracks that can be interpolated or extrapolated (polated) to the other two layers. The residual of track i , Δ_i is defined as,

$$\Delta_i = y_{i,hit} - y_{i,track}, \quad (4.2)$$

where $y_{i,hit}$ is the recorded hit position and $y_{i,track}$ is the polated track position built from hits on the two reference layers. Track residuals are affected by the local offset in the area of each layer's hit. As an example, in figure 4.4, the residual on layer 2 perhaps indicates that layer 2 is offset with respect to layers 1 and 4 in the area of the track. Of course, a single track residual says nothing of the real relative local offset because of the limited spatial resolution of the detectors and fake tracks caused by noise or delta rays. However, the mean of residuals for all tracks in a region will be shifted systematically by the local offsets between layers [31]. For a perfectly aligned quadruplet, the mean of residuals should be zero in all regions and for all reference frames, unlike the example regions in figure 4.5.

The residual distributions were wider for tracking combinations where the extrapolation lever arm was largest. In general, residual means calculated with geometrically less favourable tracking combinations have larger statistical and systematic uncertainties. The bin size of 200 μm for the distributions shown in figure 4.5 was chosen based on the uncertainty on residuals calculated from tracks on layer 4 (1) built from hits on layers 1 and 2 (3 and 4) given a cluster y-position uncertainty of 60 μm (appendix A.3), since these tracks yield residuals with the largest uncertainties.

A gaussian fit was used to extract the mean of the residual distributions. Theoretically, a double gaussian distribution is more apt, but for this analysis the gaussian fit was sufficient, as discussed in appendix C.1.

The area of the region of interest was 100 mm by 100 mm. The size balanced the amount of tracks falling in the region of interest to give sufficient statistics to the local residual distributions, while being smaller than the order on which misalignments were expected to effect the local offsets significantly. "Significantly" in this context was defined based on the distance in x that a large but possible rotation of 1000 μrad would change the local offset by more than 50 μm , which is half the required position resolution of the sTGCs [5].

It is only possible to calculate relative local offsets with cosmics data because there was no external reference to measure positions on all layers with respect to. As an example, assuming that the residual on layer 2 in figure 4.4 is representative of the relative local offset, the residual on layer 2 could be caused by layer 2 being misaligned from nominal, but it could also be caused by layers 1 and 4 being misaligned from nominal while layer 2 is in its expected position! Any number of combinations of local offsets on layers 1, 2 and 4 could produce the residual on layer 2. The value of relative local offset measurements will be shown and discussed throughout this work.

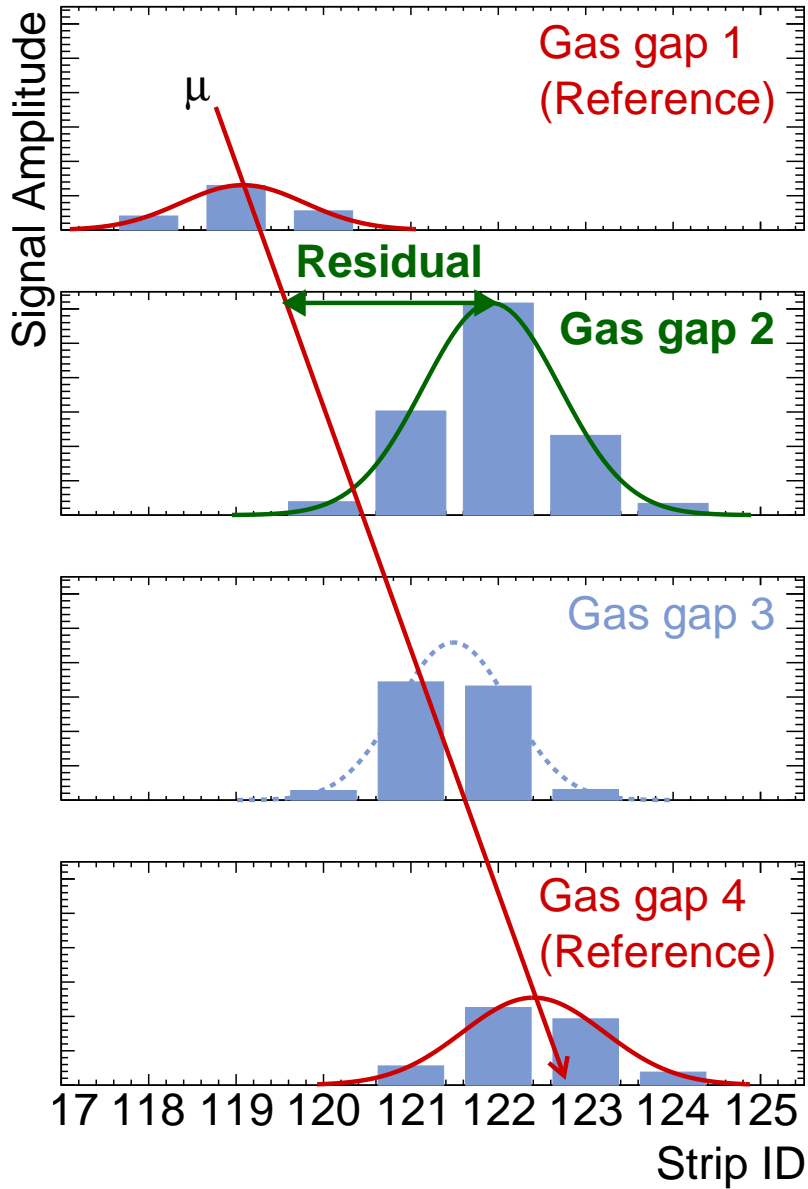
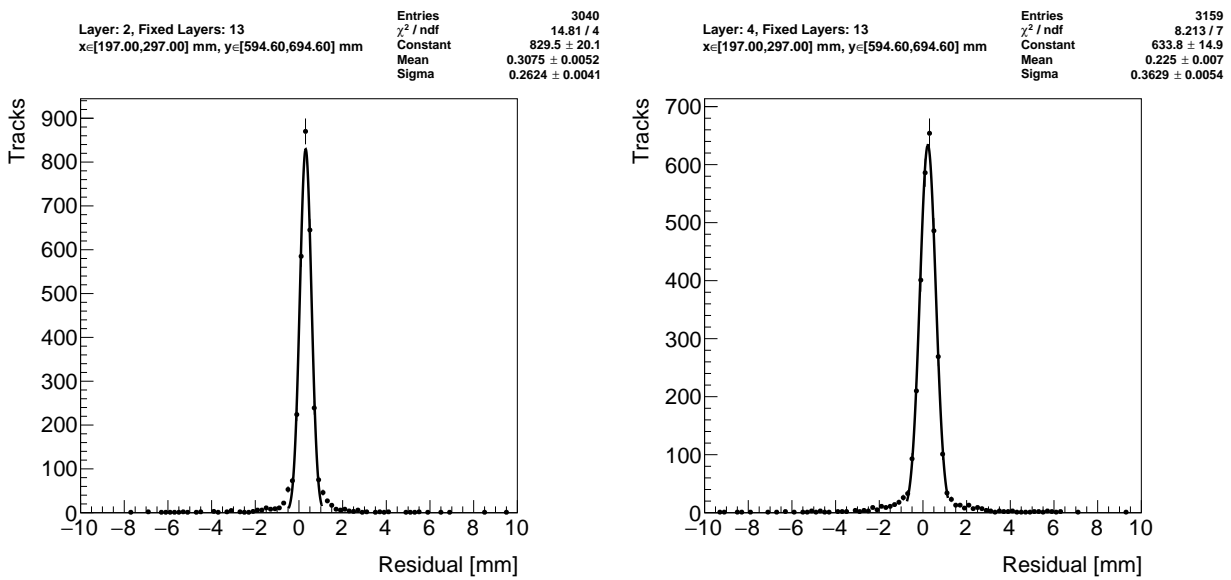


Figure 4.4: Representation of a muon event recorded by an sTGC. The clusters are fit with a Gaussian and the mean is taken as the hit position. A track is built from the chosen reference layers, 1 and 4, and the residual calculated on layer 2. The clusters come from a real muon event, but their positions were modified to highlight the residual on layer 2.



(a) Tracks on layer 2, reference layers 1 and 3. (b) Tracks on layer 4, reference layers 1 and 2.

Figure 4.5: Residual distribution in the region $x \in [197, 297] \text{ mm}, y \in [594.6, 694.6] \text{ mm}$ (100 mm by 100 mm area) for two different tracking combinations.

4.4 Visualizing relative misalignments between layers

The mean of residuals was extracted for regions across entire quadruplet layers for every tracking combination to get a picture of the relative misalignments between layers.

Figure 4.6 contains the mean of residuals on layers 2 and 4 with tracking reference layers 1 and 3. Many of the residual means are non-zero, and change smoothly over the layer, indicating that there are relative misalignments. Given that the residual mean changes with x in figure 4.6a, there is likely a rotation of layer 2 with respect to layers 1 and 3, combined with an offset of the entire layer. For layer 4 in figure 4.6b, perhaps there is a scaling [8] of the strip pattern with respect to layers 1 and 3. The interpretation of the patterns in the residual means depends on the choice of misalignment model.

4.5 Systematic uncertainty in cosmic residual means

The statistical uncertainty on the local residual means was typically around 10 - 20 μm , and appendix B shows that the analysis was not statistically limited by the number of triggers collected for each quadruplet. The systematic uncertainties were more significant.

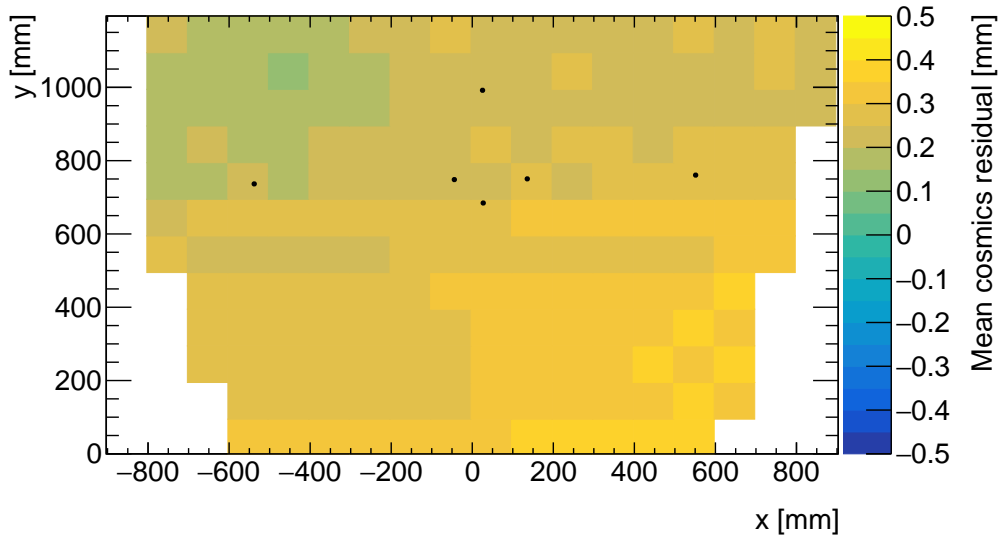
Systematic uncertainties were assigned per tracking combination as the RMS of the distribution of the difference in local residual means each calculated with a different analysis choice. For example, the RMS associated with fitting the local residual distributions with a Gaussian or double Gaussian is 25 μm for the geometrically least favourable tracking combinations and the distribution is shown in appendix C.1. For geometrically similar tracking combinations (like: tracks on layer 1 built from hits on layers 3 and 4, and tracks on layer 4 built from hits on layers 1 and 2), the systematic uncertainty was assigned as the average RMS for both.

Other choices were whether to use data collected at 2.9 kV or 3.1 kV; what cluster fitting algorithm to use; and whether or not to apply a differential non-linearity (DNL) correction to the cluster y-positions. A systematic uncertainty was assigned using the method above to account for the effect of each choice. The reasons for each choice are listed below.

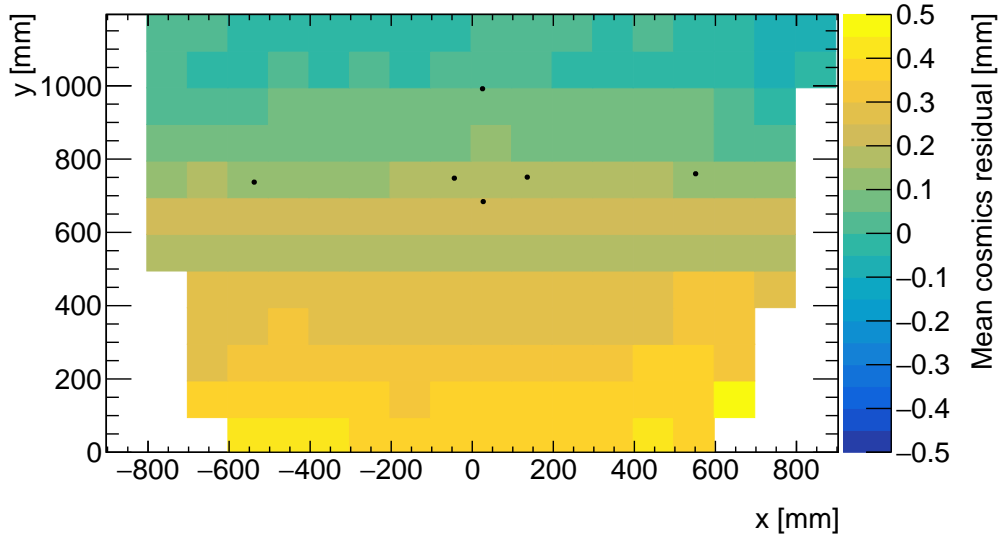
Data taken at 3.1 kV was used over 2.9 kV because the strip and wire tracking efficiency increases with higher voltage [31] (appendix C.2).

The Minuit2 package [37] was used to fit clusters over Guo's method [38] because it provided automatic statistical uncertainty estimates and is the standard choice (appendix C.3).

The DNL correction was not applied because its effect on the residual means was negligible (appendix C.4).



(a) Mean of residuals for tracks on layer 2, reference layers 1 and 3.



(b) Mean of residuals for tracks on layer 4, reference layers 1 and 3.

Figure 4.6: Mean of residuals in each 100 mm by 100 mm bin over the area of the quad layer for QL2.P.11. The black points represent x-ray survey positions, discussed in chapter 6.

Tracking geometry	Residual distribution fit function (C.1)	Cosmics data collection voltage (C.2)	Cluster fit algorithm (C.3)	Apply DNL correction or not (C.4)	Total
Layer 3, fixed layers 1, 2 - like	0.01	0.04	0.02	0.01	0.05
Layer 4, fixed layers 1, 2 - like	0.03	0.01	0.03	0.01	0.10
Layer 2, fixed layers 1, 3 - like	0.01	0.02	0.01	0.000	0.03
Layer 4, fixed layers 1, 3 - like	0.01	0.04	0.01	0.01	0.04
Layer 2, fixed layers 1, 4 - like	0.01	0.04	0.01	0.01	0.04

Table 4.1: Systematic uncertainty assigned for each analysis option, detailed in appendix [C](#).

A summary of the systematic uncertainties assigned for each tracking combination is given in table [4.1](#).

The uncertainty in each mean cosmics residual was assigned as the sum in quadrature of the statistical uncertainty in the mean and the appropriate systematic uncertainty for the tracking combination. Given that the uncertainty in the mean cosmics residuals is lesser than or near to the order of the required position resolution of the sTGCs (100 μm [\[5\]](#)) the cosmic residual means are relevant input for alignment studies.

Chapter 5

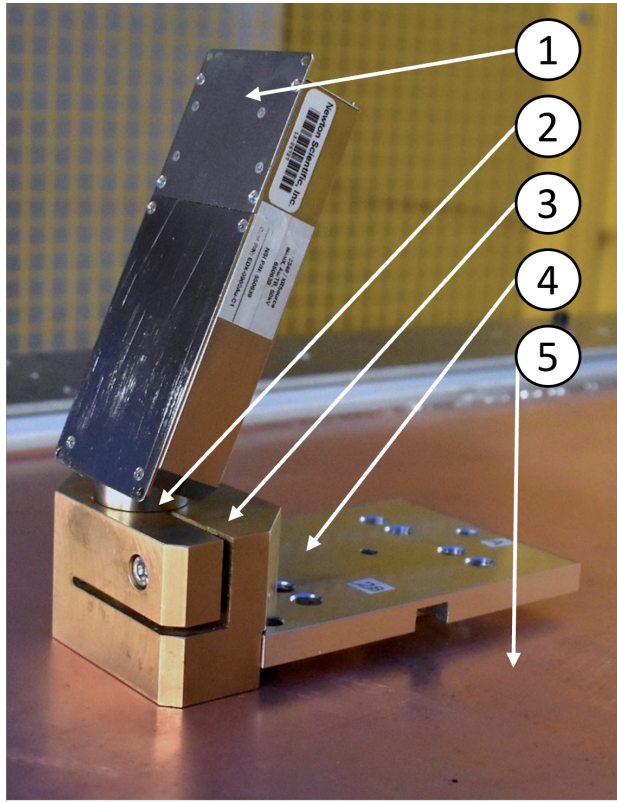
Using x-rays to measure relative strip position offsets

Work on characterizing relative misalignments between quadruplet layers is ongoing [39], (Can I cite John's thesis-in-progress?) but what is required are the absolute strip positions with respect to their nominal position in the ATLAS analysis coordinate system to be input into Athena [40]. Somehow, absolute misalignment parameters must be derived to create a model of absolute strip positions - which is not possible with the cosmics dataset. Absolute local offset measurements were done by the so-called x-ray method [9]. The x-ray tests were performed after the quadruplets arrived at CERN and were assembled into wedges. Essentially, an x-ray gun was attached to one of the source plates glued to the surface of the wedge (figure 5.1), and the beam profile recorded by the strips.

The gun produced x-rays of 7 - 15 keV that were collimated before reaching the surface of the wedge. The x-rays mostly interacted with the wedge's copper electrodes and gold-plated tungsten wires via the photo effect. The resulting photoelectrons caused ionization avalanches. The beam profile was captured by the distribution of cluster positions. A typical beam profile is shown in figure 5.2.

Clusters with signal on more than 5 strips were cut because they were most likely caused by photoelectrons ejected with enough energy to cause more primary ionization and subsequent avalanches (δ -rays) [9].

The mean of the cluster position distribution was taken as the x-ray beam profile center. The expected center was calculated assuming a wedge with nominal geometry given the gun position. The difference between the expected and reconstructed beam profile center is a measure of the local offset. Applying the logic of equation 4.1 to the beam profile, the fitted



1. X-ray gun
2. Collimator
3. Gun mount
4. Base plate (attached to source plate underneath)
5. sTGC wedge surface

Figure 5.1: The x-ray gun mounted to the alignment platform on the surface of the wedge.
Adapted from ©CERN for the benefit of the ATLAS collaboration. CC-BY-4.0 license.

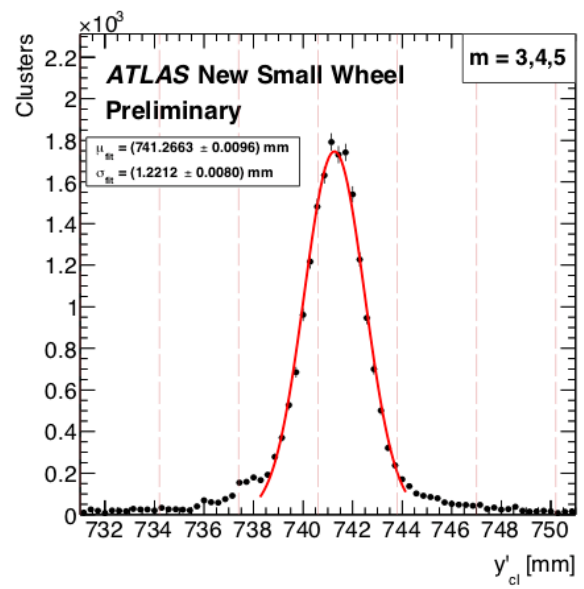


Figure 5.2: Distribution of x-ray cluster mean positions after the analysis cuts and corrections. The strip cluster multiplicity, m , was limited to 3, 4 and 5. The red line is a Gaussian fit of the distribution and the pink lines denote the edges of the strips. Adapted from ©CERN for the benefit of the ATLAS collaboration. CC-BY-4.0 license.

mean acts as y , the expected center is y_{nom} and the local offset is d_{local} as before. The x-ray local offsets give the absolute local position of the strip pattern with respect to the source plates. Since the position of the source plates will be monitored by the alignment system in ATLAS [5], the local position of the strip pattern can be known in the ATLAS coordinate system for every position where x-ray data was taken.

The main advantage of the x-ray dataset over the cosmics dataset is that absolute local offsets are measurable thanks to the reference frame provided by the source plates. However, the systematic uncertainty on the x-ray offsets is large: 120 μm was accepted by the collaboration. The cuts and corrections applied to the x-ray data that motivate the uncertainty are detailed in Lefebvre, 2020 [9]. In addition, local offset measurements were limited to the positions of the alignment platforms; only 10 - 20 positions were surveyed for each wedge. Therefore, validating the x-ray measurements and seeing how they can be improved is important because of the uncertainty in and incompleteness of the dataset. How the cosmics dataset was used for this purpose is discussed in chapter 6.

Chapter 6

Comparing cosmic muon and x-ray relative strip position offsets

The goal was to validate the local offsets extracted from the x-ray data with cosmics data. The complication was that the x-ray dataset provided absolute local offsets while the cosmics dataset provided relative local offsets, which could not be compared directly. The solution was to analyze the x-ray data in the same relative coordinate system as the cosmics data. The methods and results of the comparison are presented here.

6.1 Method for comparing x-ray and cosmics data

The measured x-ray beam profile centers were systematically affected by local offsets in the same way as the mean cosmics residuals, as modeled by equation 4.1. Therefore, if a 2-layer track is abstracted from the beam profile centers on each layer and the residual calculated on a third layer, that residual should match the local mean cosmics residual.

The track is "abstracted" because a so-called "beam profile center" is actually the Gaussian mean of all selected mean cluster positions recorded during the x-ray data taking period. Abstracting a track was necessary because the x-rays cause signal in the chamber via the photoeffect so there were not individual "x-ray tracks" to record. In fact the x-ray data was collected separately for each layer. Nonetheless, since the effect of local offsets on the beam profile centers was the same the difference in algorithm between x-ray and cosmics analysis was allowed.

For each x-ray survey position, the x-ray residual was calculated for all possible tracking combinations (which required an x-ray beam profile on at least three layers). The position

of the x-ray residuals are shown as black dots over figure 4.6a and 4.6b. Note that the mean of cosmics residuals around the x-ray points were calculated in bins exactly centered on the nominal x-ray gun position, unlike in figure 4.6.

6.2 Assessing correlation

Scatter plots of the x-ray and mean cosmics residuals for two sample quadruplets in figures 6.1 and 6.2 reveal the degree of correlation between the datasets.

First, the fitted slope and offset in figure 6.1 show that the two QL2.P.11 datasets are correlated. However, the magnitude of the uncertainties in the x-ray residuals is large (up to half a millimeter) since it comes from propagating the 120 μm uncertainty in the beam profile centers. The large uncertainty set a limit on the sensitivity of the analysis, for if the absolute value of the x-ray residuals of a quadruplet were smaller than the x-ray residual uncertainties, no conclusion about the correlation could be drawn, like for QL2.P.8 (figure 6.2).

Several quadruplets were tested for each quadruplet construction geometry built in Canada: QL2P, QL2C, and QS3P. Each quadruplet fell into one of the two categories: residuals large enough to see a correlation, or residuals too small to see a correlation. Since the x-ray and mean cosmics residuals were measures of the relative local offsets between the layer of a quadruplet and the two reference layers, quadruplets with the most relative misalignment had the largest range of residuals. So, the correlation plots were an easy visual way to identify quadruplets with large relative misalignments.

There are three patterns in the residuals on the scatter plot explained by geometry. First, for both datasets the uncertainty in the extrapolated track residuals were larger than the interpolated track residuals because of the extrapolation lever arm. For the x-ray residuals, the effect of the lever arm on the uncertainty was direct since the residual was calculated from a single abstracted track; for the cosmics residuals it was the widening of the residual distribution on the layer of interest due to the extrapolation lever arm that increased the statistical uncertainty in the fitted mean of residuals. Second, residuals calculated through extrapolation tend to be larger because the extrapolation lever arm can produce more extreme values. Third, the pattern of points in figure 6.1 is slightly mirrored. This is expected since the residuals calculated for a given set of three layers are geometrically correlated.

The correlation of the cosmics residuals with the x-ray residuals alone does not validate the method; all the studies in described in appendices B and C demonstrate its robustness. The analysis could be validated externally by comparing the mean cosmics residuals to the relative misalignment parameters calculated using `tgc_analysis/MatrixMethod` [35] and JOHN FLORES CHI2 METHOD.

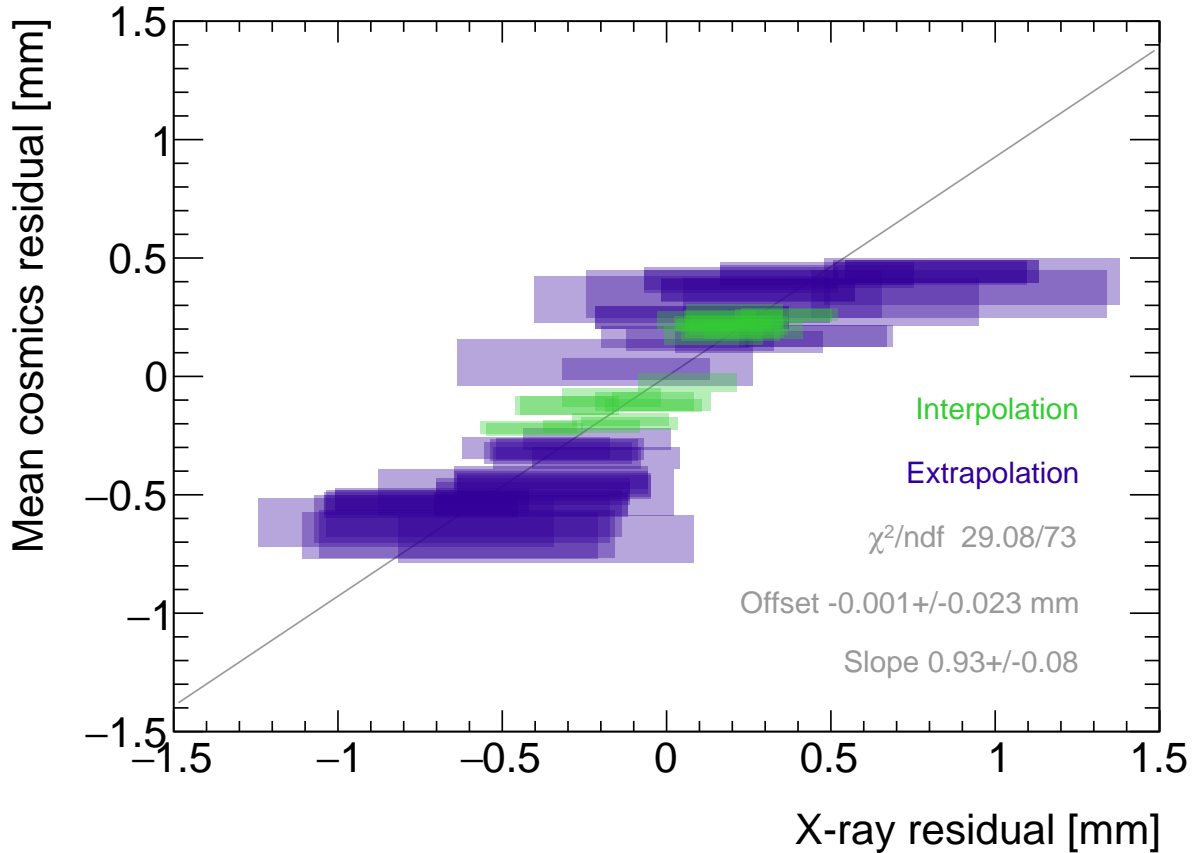


Figure 6.1: Correlation plot between x-ray and cosmics residuals for all tracking combinations for QL2.P.11. Each rectangle is centered on an x-ray and mean cosmics residual pair. The width of the rectangles in x and y are the uncertainty in the x-ray and mean cosmics residual respectively. A printer-friendly version of this plot is available in appendix D.

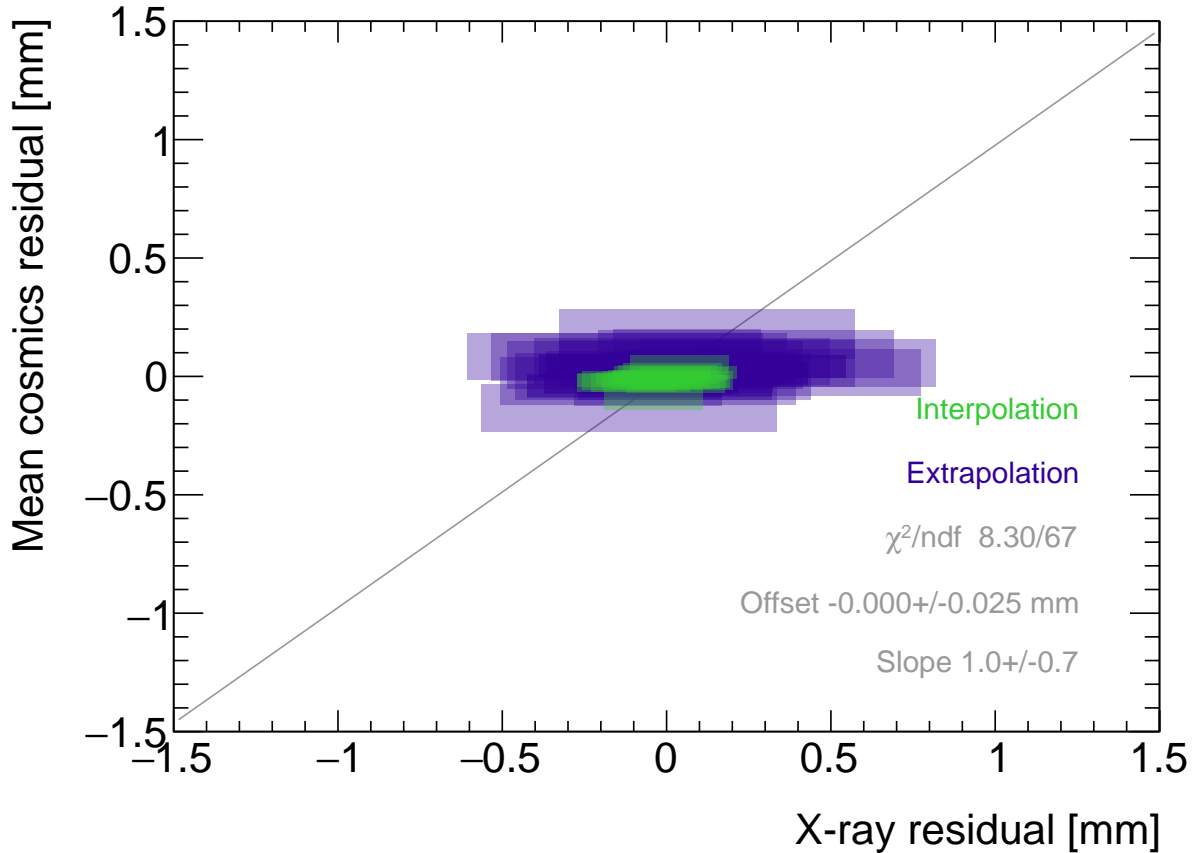


Figure 6.2: Correlation plot between x-ray and cosmics residuals for all tracking combinations for QL2.P.8. Each rectangle is centered on an x-ray and mean cosmics residual pair. The width of the rectangles in x and y are the uncertainty in the x-ray and mean cosmics residual respectively. A printer-friendly version of this plot is available in appendix D.

6.3 Limitations

The most important limit on measuring the degree of correlation between the x-ray and cosmics residuals was the uncertainty on the x-ray residuals, which stemmed from the systematic uncertainty in the x-ray beam profile centers [9]. The method was limited primarily by the sTGCs' poor x-ray position resolution, since x-rays do not create real tracks anyways.

The analysis of certain quadruplets was also limited by the availability of data. Sometimes, less than three layers were surveyed for a given x-ray gun position so no residuals could be calculated. Too few x-ray residuals prevented the analysis from detecting a significant correlation. Often, the analysis of smaller quadruplets suffered as a result because they had fewer alignment platforms, and hence gun positions, on their surfaces. In addition, the analysis was limited to certain quadruplets. The wedges constructed the earliest (typically small wedges) were surveyed when the method was still being designed and so have limited x-ray residuals calculated from beam profiles of lower quality. Also, not all cosmic muon test sites had enough front end electronics to collect data on three layers simultaneously, which is the minimum required to be able to calculate residuals.

Nonetheless, the comparison of x-ray and cosmics residuals was really to confirm the x-ray method's ability to measure local offsets with an independent dataset; the analysis of quadruplets with relative misalignments large enough to detect a correlation achieved this goal.

Chapter 7

Outlook

The cosmic muon dataset can be used to independently confirm the absolute local offsets measured by the x-ray method. They are being used to complete the sTGC alignment scheme of the NSWs: the NSW alignment system monitors the position of alignment platforms on the surface of sTGC wedges, and the x-ray measurements provide the offsets of the strip pattern with respect to each alignment platform. The continuation of this analysis is detailed next (section 7.1) before considering the larger context (section 7.2).

7.1 Next steps

Next all quadruplets with suitable cosmics and x-ray data should be surveyed to flag anomalous quadruplets (as a first step). If a quadruplet’s correlation plot like figure 6.1 or 6.2 reveals an unexpected correlation or has a large scatter, it would indicate an issue with either the cosmics or x-ray data collection to be investigated further. The uncertainty in each set of tracking points would inform the interpretation of the anomaly. Then, the quality of the correlation should be evaluated over all quadruplets instead of individually.

For now, the correlation for the individual quadruplets tested support the use of the x-ray data to build a global misalignment model [9]. Work on creating a misalignment model is ongoing with the development of `stgc_as_built_fit` [41]. Currently, the algorithm compares the y-position of a local group of strips at each x-ray gun position as measured by the x-ray and CMM methods in a fit to extract a global slope (m) and offset (b) per layer, l , where the χ^2 is given by equation 7.2.

$$dy_{cmm,corr} = y_{cmm} + b_l + m_l x - y_{nom} \quad (7.1)$$

$$\chi^2 = \frac{[dy_{cmm,corr} - dy_{xray}]^2}{\delta dy_{xray}^2 + \delta dy_{cmm,corr}^2} \quad (7.2)$$

Here, dy refers to the corrected CMM and x-ray local offsets, and δdy refers to their respective uncertainties. The CMM measurements were taken before the cathode boards were assembled into quadruplets, so alignment parameters for the given layer were extracted from the χ^2 fit by stepping the corrected CMM y-position towards the x-ray y-position by adjusting the alignment parameters. The plan is that the alignment parameters will be provided to [Athena](#) [40] to precisely reconstruct muon tracks from the NSWs' sTGCs.

Figure 6.1 and 6.2 clearly show that the uncertainty in the mean cosmics residuals was much smaller than the uncertainty in the x-ray residuals. It was the result of the uncertainty in the cosmic muon hit positions on each layer being smaller than the uncertainty on the x-ray beam profile centers (60 μm versus 120 μm). Therefore, it would be great to use the cosmics residuals as input to calculate and reduce the uncertainty on the alignment parameters. Since mean cosmics residuals can only provide relative misalignment information, one idea would be to use them to constrain the fit of the alignment parameters. In this case, the alignment parameters would need to be fitted on all layers at once, and the shifting y-positions on each layer forced to create an abstracted track residual equal to the local mean cosmics residual (within uncertainty) for each x-ray point. Or, instead of constraining the fit, it could be penalized if the resulting parameters do not result in abstracted track residuals equal to the mean cosmics residuals within uncertainty. Some work on using the three datasets at once in a fit has begun but has prompted the idea to compare just the cosmics and CMM data first.

7.2 Importance in context

Ultimately, the positions of the sTGC strip electrodes need to be known in ATLAS to within 100 μm so that they can provide the required position resolution for the High-Luminosity LHC. The x-ray measurements will account for misalignments between strip layers to achieve this goal. The cosmics dataset was used to confirm the local offsets measured with the x-ray gun, and could be used to improve the misalignment model that will position each strip.

Achieving the required position resolution on each layer of the NSWs in the particle track bending plane achieves the design momentum resolution for muons ejected towards the end-caps of ATLAS. Muons are important signatures of electroweak and Higgs sector events of interest for the ATLAS Collaboration's future physics goals [5]. Being the second of two tracking technologies on the NSWs, an effective misalignment model of sTGC quadruplets is

a necessary part of making the NSWs redundant for 10 or more years of recording collisions in the High Luminosity era of the LHC.

References

- [1] G Apollinari, I Bejar Alonso, O Bruning, P Fessia, M Lamont, L Rossi, and L Tavian. High-Luminosity Large Hadron Collider (HL-LHC) Technical Design Report V. 0.1. Technical report, CERN, Geneva, September 2017.
- [2] L Evans and P Bryant. LHC Machine. *Journal of Instrumentation*, 3(S08001), 2008.
- [3] A Dainese et al. The physics potential of HL-LHC. In *Input to the European Particle Physics Strategy Update*, November 2018.
- [4] The ATLAS Collaboration. The ATLAS Experiment at the CERN Large Hadron Collider. *Journal of Instrumentation*, 3(08):S08003, 2008.
- [5] T Kawamoto, S Vlachos, L Pontecorvo, J Dubbert, G Mikenberg, P Iengo, C Dallapiccola, C Amelung, L Levinson, R Richter, and D Lellouch. New Small Wheel Technical Design Report. Technical report, Jun 2013. ATLAS New Small Wheel Technical Design Report.
- [6] Angel Abusleme et al. Performance of a Full-Size Small-Strip Thin Gap Chamber Prototype for the ATLAS New Small Wheel Muon Upgrade. *Nuclear Instruments and Methods in Physics Research Section A: Accelerators, Spectrometers, Detectors and Associated Equipment*, 817:85–92, May 2016. arXiv: 1509.06329.
- [7] E. Perez Codina. Small-strip Thin Gap Chambers for the muon spectrometer upgrade of the ATLAS experiment. *Nuclear Instruments and Methods in Physics Research Section A: Accelerators, Spectrometers, Detectors and Associated Equipment*, 824:559–561, July 2016.
- [8] Evan Michael Carlson. *Results of the 2018 ATLAS sTGC test beam and internal strip alignment of sTGC detectors*. Thesis, University of Victoria, Victoria, Canada, 2019. Accepted: 2019-07-16T17:20:40Z.

- [9] B. Lefebvre. Precision survey of the readout strips of small-strip Thin Gap Chambers using X-rays for the muon spectrometer upgrade of the ATLAS experiment. *Journal of Instrumentation*, 15(07):C07013–C07013, July 2020.
- [10] P.A. Zyla et al. Review of Particle Physics. *PTEP*, 2020(8):083C01, 2020.
- [11] ATLAS luminosity public results run-1, March 2011.
- [12] ATLAS luminosity public results run-2, July 2015.
- [13] The European Strategy for Particle Physics. Technical Report CERN/2685, CERN, 2006. Adopted by the CERN council at a special session at ministerial level in Lisbon in 2006.
- [14] HiLumi HL-LHC Project. LHC/HL-LHC plan (last update january 2021). <https://hilumilhc.web.cern.ch/content/hl-lhc-project>, last accessed on 2021-09-09.
- [15] ATLAS inner detector : Technical Design Report, 1. Technical Report CERN-LHCC-97-016, CERN, 1997. ISBN: 9789290831020 Publication Title: CERN Document Server.
- [16] L. Rossi, S. Haywood, A. Romanouk, and R. Nickerson. ATLAS inner detector : Technical Design Report, 2. Technical Report CERN-LHCC-97-017, CERN, 1997. ISBN: 9789290831037 Publication Title: CERN Document Server.
- [17] ATLAS liquid-argon calorimeter : Technical Design Report. Technical Report CERN-LHCC-96-041, CERN, 1996. ISBN: 9789290830900 Publication Title: CERN Document Server.
- [18] ATLAS tile calorimeter : Technical Design Report. Technical Report CERN-LHCC-96-042, CERN, 1996. ISBN: 9789290830917 Publication Title: CERN Document Server.
- [19] ATLAS level-1 trigger : Technical Design Report. Technical Report CERN-LHCC-98-014, CERN, 1998. ISBN: 9789290831280 Publication Title: CERN Document Server.
- [20] Marzio Nessi, Markus Nordberg, Peter Jenni, and Kenway Smith. ATLAS high-level trigger, data-acquisition and controls : Technical Design Report. Technical Report CERN-LHCC-2003-022, CERN, 2003. Publication Title: CERN Document Server.
- [21] A Ruiz Martínez and. The run-2 ATLAS trigger system. *Journal of Physics: Conference Series*, 762:012003, oct 2016.
- [22] ATLAS magnet system : Technical Design Report, 1. Technical Report CERN-LHCC-97-018, CERN, 1997. ISBN: 9789290831044 Publication Title: CERN Document Server.

- [23] ATLAS Collaboration. Performance of the ATLAS muon trigger in pp collisions at $\sqrt{s}=8$ TeV. *The European Physical Journal C*, 75(3):120, March 2015. arXiv: 1408.3179.
- [24] ATLAS Collaboration. ATLAS Muon Spectrometer: Technical Design Report. Technical Report CERN-LHCC-97-022, CERN, Geneva, 1997.
- [25] S. Aefsky, C. Amelung, J. Bensinger, C. Blocker, A. Dushkin, M. Gardner, K. Hashemi, E. Henry, B. Kaplan, P. Keselman, M. Ketchum, U. Landgraf, A. Ostapchuk, J. Rothberg, A. Schricker, N. Skvorodnev, and H. Wellenstein. The Optical Alignment System of the ATLAS Muon Spectrometer Endcaps. *Journal of Instrumentation*, 3(11):P11005–P11005, November 2008. Publisher: IOP Publishing.
- [26] John Townsend. *Electricity in gases*. Clarendon Press, Oxford, 1915.
- [27] E. Gatti, A. Longoni, H. Okuno, and P. Semenza. Optimum geometry for strip cathodes or grids in MWPC for avalanche localization along the anode wires. *Nuclear Instruments and Methods*, 163(1):83–92, July 1979.
- [28] G. Battistoni, P. Campana, V. Chiarella, U. Denni, E. Iarocci, and G. Nicoletti. Resistive cathode transparency. *Nuclear Instruments and Methods in Physics Research*, 202(3):459–464, November 1982.
- [29] The ATLAS Collaboration. Technical Design Report for the Phase-I Upgrade of the ATLAS TDAQ System. Technical report, Sep 2013. Final version presented to December 2013 LHCC.
- [30] Technical Design Report for the Phase-II Upgrade of the ATLAS TDAQ System. Technical report, CERN, Geneva, Sep 2017.
- [31] Benoit Lefebvre. *Characterization studies of small-strip Thin Gap Chambers for the ATLAS Upgrade*. PhD Dissertation, McGill University, Montreal, Canada, 2018.
- [32] George Iakovidis. VMM3, an ASIC for Micropattern Detectors. In *Proceedings of Science*, page 5, Philadelphia, 2017.
- [33] Bohan Chen. *Calibration Studies of the Front-End Electronics for the ATLAS New Small Wheel Project*. PhD thesis, McGill University, Montreal, Canada, 2019.
- [34] R. Keyes, K.A. Johnson, L. Pepin, F. Léger, C. Qin, S. Webster, A. Robichaud-Véronneau, C. Bélanger-Champagne, B. Lefebvre, S.H. Robertson, A. Warburton, B. Vachon, and F. Corriveau. Development and characterization of a gas system and

- its associated slow-control system for an ATLAS small-strip thin gap chamber testing facility. *Journal of Instrumentation*, 12(04):P04027–P04027, April 2017.
- [35] Benoit Lefebvre. tgc_analysis.
 - [36] Fabio Sauli. Principles of operation of multiwire proportional and drift chambers. In *Cern Yellow Reports: Monographs*, page 92 p, Geneva, 1977. CERN, CERN. CERN, Geneva, 1975 - 1976.
 - [37] M. Hatlo, F. James, P. Mato, L. Moneta, M. Winkler, and A. Zsenei. Developments of mathematical software libraries for the LHC experiments. *IEEE Trans. Nucl. Sci.*, 52:2818–2822, 2005.
 - [38] Hongwei Guo. A Simple Algorithm for Fitting a Gaussian Function [DSP Tips and Tricks]. *IEEE Signal Processing Magazine*, 28(5):134–137, September 2011.
 - [39] Xiao Zhao, Wenlong Li, Dengfeng Zhang, Changyu Li, Han Li, Shengquan Liu, Peng Miao, Yanyan Du, Yanyun Duan, and Chengguang Zhu. Cosmic test of sTGC detector prototype made in China for ATLAS experiment upgrade. *Nuclear Instruments and Methods in Physics Research Section A: Accelerators, Spectrometers, Detectors and Associated Equipment*, 927:257–261, May 2019.
 - [40] The ATLAS Collaboration. Athena.
 - [41] Benoit Lefebvre. stgc_as_built_fit.
 - [42] Ichita Endo, Tatsuo Kawamoto, Yoshinari Mizuno, Takashi Ohsugi, Takashi Taniguchi, and Tohru Takeshita. Systematic shifts of evaluated charge centroid for the cathode read-out multiwire proportional chamber. *Nuclear Instruments and Methods in Physics Research*, 188(1):51–58, September 1981.
 - [43] S. Majewski, G. Charpak, A. Breskin, and G. Mikenberg. A thin multiwire chamber operating in the high multiplication mode. *Nuclear Instruments and Methods*, 217:265–271, 1983.
 - [44] Bernd Stelzer. The New Small Wheel Upgrade Project of the ATLAS Experiment. *Nuclear and Particle Physics Proceedings*, 273-275:1160–1165, April 2016.
 - [45] Manfred Krammer. Upgrade Programs of the LHC Experiment, November 2017.
 - [46] Lia Formenti. cosmics_xray_correlation.
 - [47] Siyuan Sun. sTGC_readout_sw.

[48]

- [49] G Brianti. Large Hadron Collider in the LEP Tunnel. In *Proceedings of the ECFA-CERN Workshop*, volume 1, page 352, Lausanne and Geneva, March 1984.
- [50] Letter of Intent for the Phase-I Upgrade of the ATLAS Experiment. Technical Report CERN-LHCC-2011-012. LHCC-I-020, CERN, Geneva, November 2011.
- [51] ATLAS: letter of intent for a general-purpose pp experiment at the large hadron collider at CERN. Technical Report CERN-LHCC-92-004, CERN, Geneva, 1992.

APPENDICES

Appendix A

Uncertainty in cluster positions

A.1 Cluster definition

A cluster is a series of contiguous strip channels on a layer with non-zero amplitude, all part of the same trigger and having the same event number [31]. Clusters result from the drift of ionization products generate in the ionization avalanche caused by a muon [26]. The peak-detector-output (PDO) of the signal on each strip of a cluster is fit with a Gaussian. The y-position of a particle as it passed through the layer is mean of the cluster, referred to here as the hit position.

A.2 Effect of fit algorithm on cluster mean

The clusters were fit with Guo's method [38] and Minuit2 for ROOT [37]. The difference in cluster means between the two algorithms is shown in figure A.1.

The RMS of the distribution in figure A.1 is 57 μm , which is much larger than the statistical uncertainty in the mean for the Minuit2 algorithm, which peaks around 7 μm . An RMS of 60 μm is common for data taken with most quadruplets at 3.1 kV. Therefore, the uncertainty in the y-hit positions is assigned 60 μm .

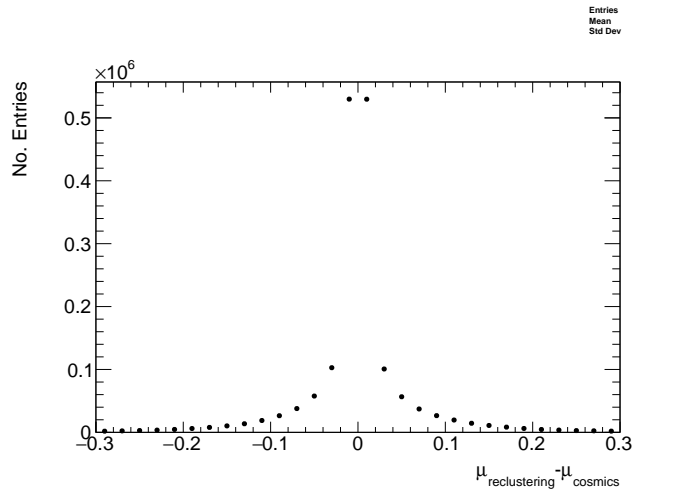


Figure A.1: The difference between cluster means calculated with Guo’s method [38] in `tgc_analysis/CosmicsAnalysis` and `Minuit2` for `ROOT` [37] in `strip_position_analysis/ReClustering` for data collected with QL2.P.8 at 3.1 kV.

A.3 Effect of uncertainty in cluster mean on track residuals

The uncertainty assigned to the hit position affected the uncertainty in the extrapolated/interpolated position of the track, and in the residuals. The bin size of the residual distributions was set to 200 μm because that was the uncertainty in the residuals calculated from the tracks with the least favourable geometry (like tracks built from hits on layers 1 and 2 and extrapolated to layer 4).

Appendix B

Study of cosmics for alignment analysis statistical uncertainty

Typically, one million triggers (cosmic muon events and noise) were collected for each Canadian quadruplet at McGill University, resulting in roughly half the number of viable tracks after cuts in `tgc_analysis/CosmicsAnalysis`. For QS3.P.18, 3.5 million triggers were collected. To gauge the sensitivity of the analysis to the available statistics, partitions of this data with each with a different number of triggers were analyzed separately. Ultimately, the quantity of interest was the gaussian mean of the residual distribution in regions of interest, so the peak in the distribution of the statistical uncertainty in the residual means for each area of interest for a specific tracking combination was used to gauge the quality of the analysis. How the peak in the residual mean uncertainty distribution changes with the number of triggers is shown in figure for tracks on layer 1 built from layers 3 and 4 [B.1](#).

The uncertainty is already around $20\text{ }\mu\text{m}$ at 1 million triggers, suitable for distinguishing differences in offsets of order $50\text{ }\mu\text{m}$ as required. Although increased statistics could decrease the statistical uncertainty, it is not required for the goals of this analysis. Moreoever, the systematic uncertainty is around $50\text{ }\mu\text{m}$ and the systematic uncertainty on the x-ray residuals is $150\text{ }\mu\text{m}$ so the statistical uncertainty of $20\text{ }\mu\text{m}$ is nearly negligible.

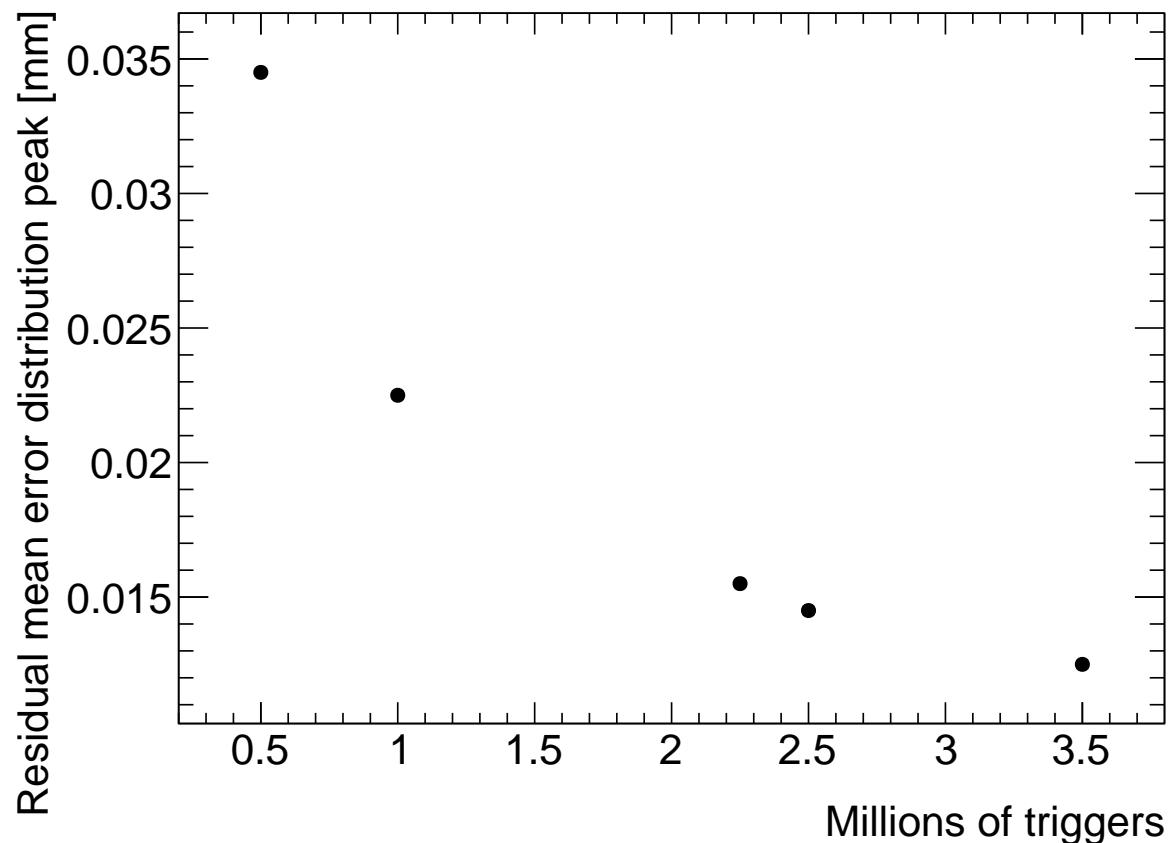


Figure B.1: How the peak of the distributions of uncertainties in the residual means in regions of interest for tracks on layer 1 built from layers 3 and 4 changed with the number of triggers used in the analysis. The distribution falls off as $\frac{1}{\sqrt{N}}$ as expected.

Appendix C

Study of systematic uncertainties when using cosmics data for alignment studies

C.1 Residual distribution fit function

The distribution of residuals should be modelled by a double gaussian fit[31]:

$$G(r) = A_s \exp\left[\frac{-(r - \mu)^2}{2\sigma_s^2}\right] + A_b \exp\left[\frac{-(r - \mu)^2}{2\sigma_b^2}\right] \quad (\text{C.1})$$

where r is the residual, A is the gaussian amplitude, μ is the gaussian mean, σ is the gaussian sigma, and the subscripts s and b stand for signal and background respectively. One gaussian captures the real (signal) tracks and the other captures the tracks built from noise (background). The gaussian with the smaller width is identified as the signal.

A single gaussian fit failed less often than a double gaussian fit. The gaussian fits were performed by initially estimating the amplitude to be 100 tracks, the gaussian mean to be the histogram mean, and gaussian σ to be the RMS. The fit range was restricted to ± 1 RMS from the histogram mean. The modification helped the gaussian fit capture the signal peak. An example residual distribution is shown in figure C.1.

For all residual distributions in 100 mm by 100 mm bins on layer 4 built from hits on layers 1 and 2, the difference in gaussian and double gaussian means and σ 's is shown in figure C.2. Since the RMS of the residual mean differences distribution is less than 50 μm the gaussian

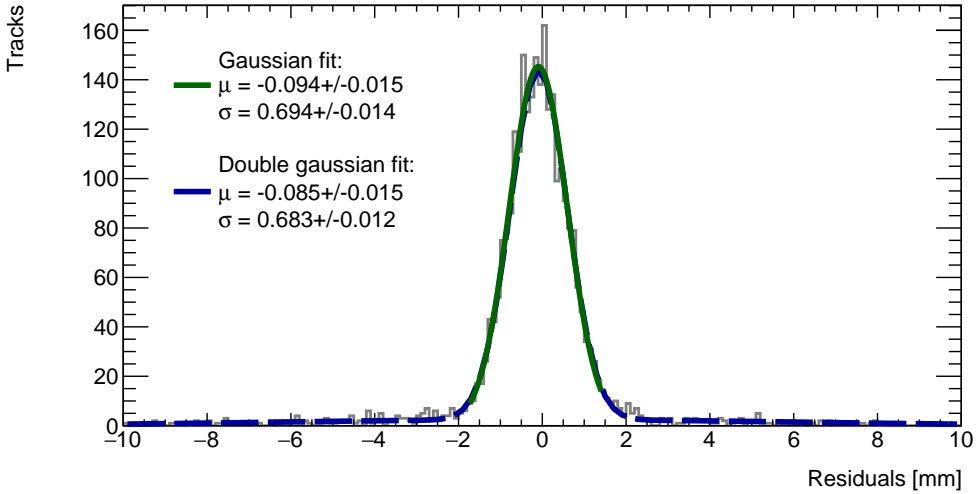


Figure C.1: Residual distribution for tracks on layer 4 built from hits on layers 1 and 2 for $x \in [-3.00, 97.00]$, $y \in [394.60, 494.60]$ mm for QL2.P.8 fit with a double gaussian and a single gaussian in a range of ± 1 RMS from the histogram mean.

fit gave the same result within the required precision. Moreover, this is for the tracking combination with the worst extrapolation lever arm and the widest distribution of mean differences; the interpolation combinations have narrower distributions.

The gaussian σ should be larger than the double gaussian σ because the gaussian distribution includes the effect of the noise tracks with large residuals, while the double gaussian models signal and background residuals separately. For this analysis, only the residual mean was important, so the systematic overestimate of the signal σ in the gaussian fit shown on the right of figure C.2 was allowed.

C.2 Cosmic muon data collection voltage

Cosmic muon data was collected at 2.9 kV and 3.1 kV because although 2.9 kV is closer to the operating conditions the chambers will be subject to in ATLAS, the extra gain provided by operating at 3.1 kV increased the signal to noise ratio for pad signals. Also, the tracking efficiency was higher with data collected at 3.1 kV. The difference in gain affected the relative population of clusters of different sizes, which in turn affected the uncertainty in the strip hit positions on each layer, the uncertainty in the track positions and the residual distributions. The residual distributions for 3.1 kV data are narrower, as shown in figure C.3.

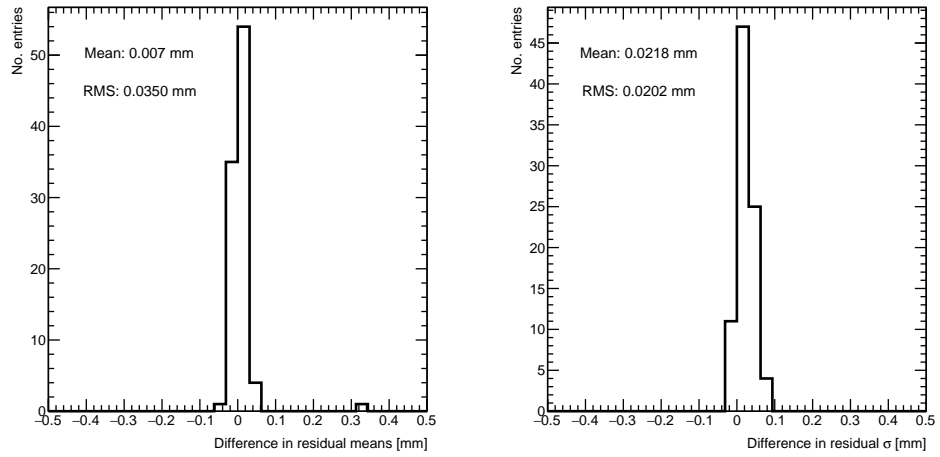


Figure C.2: Difference in residual distribution means and σ 's for a gaussian and double gaussian fit, for all residual distributions in 100 mm by 100 mm bins on layer 4 built from hits on layers 1 and 2 for QL2.P.8.

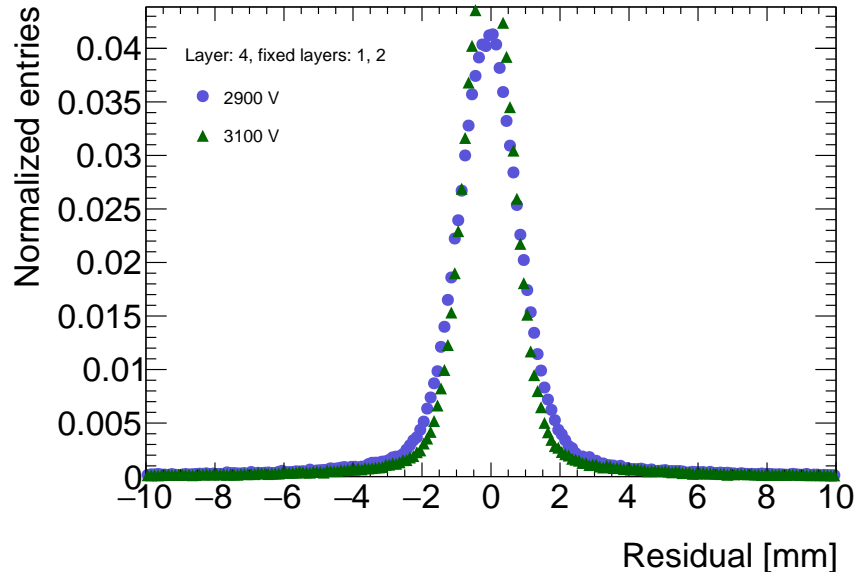


Figure C.3: Residual distribution for tracks on layer 4 built from hits on layers 1 and 2 for QL2.P.8 for data collected at 2.9 kV and 3.1 kV.

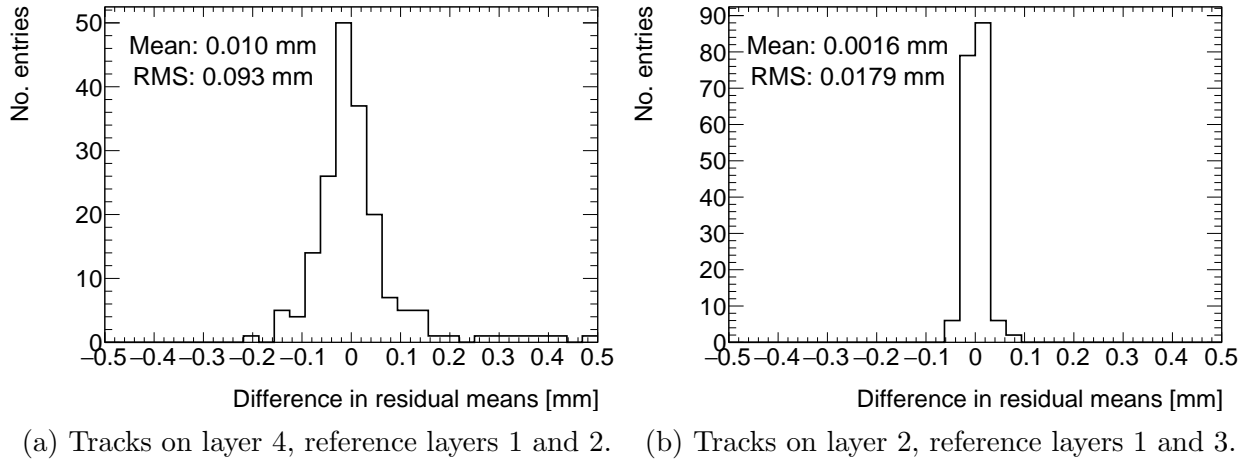


Figure C.4: Difference in residual means for data collected with QL2.P.8 at 2.9 kV and 3.1 kV respectively in 100 mm by 100 mm bins for (a) tracks on layer 4 built from hits on layers 1 and 2 and (b) tracks on layer 2 built from hits on layers 1 and 3.

Neither dataset is better for calculating the mean of residuals in a given area, so a systematic uncertainty can be assigned based on the difference in residual means calculated for 2.9 kV and 3.1 kV data; namely, the systematic uncertainty was approximated as the RMS of the residual mean difference distribution. Data taken with QL2.P.8 was used to estimate the RMS, as in figure C.4a.

Tracks built from hits on layers 1 and 2 and extrapolated to layer 4 have the worst lever arm and hence the most uncertainty. The width of the distribution for geometrically favourable tracks are much narrower. The narrowest width of the residual mean difference distribution is for tracks on layer 2 built from hits on layers 1 and 3 (see figure C.4b).

Therefore, for each tracking combination, a systematic uncertainty equal to the RMS of the residual mean difference distribution was assigned.

C.3 Cluster fit algorithm

To ensure that changing the cluster fitting algorithm like in appendix A would not change the calculated mean of residuals in each region of interest significantly, the residual means were compared in both cases. The distribution of the difference in residual means is plotted in figure C.5 for the tracking combination with the worst extrapolation lever arm.

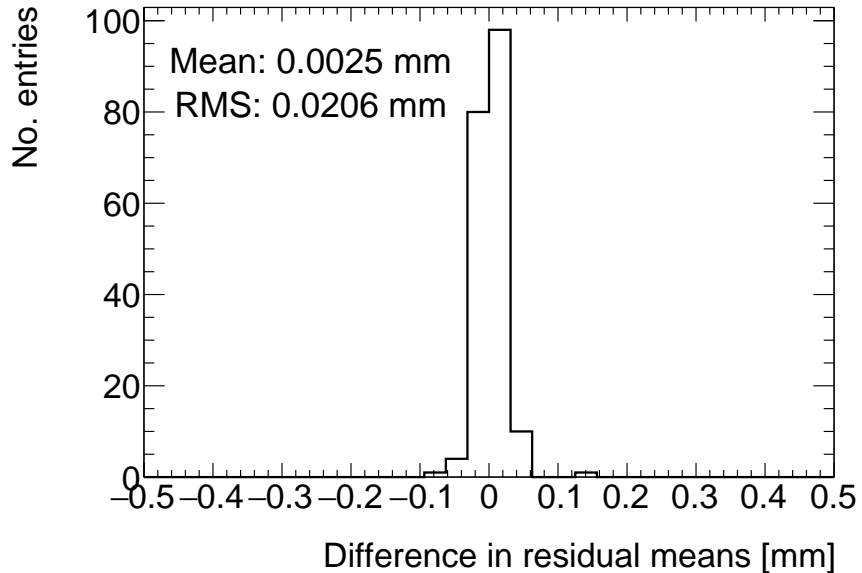


Figure C.5: Difference in residual means when the cluster fit algorithm is `Minuit2` [37] versus Guo’s method [38] for tracks on layer 4 built from hits on layers 1 and 2 for QL2.P.8.

The other tracking combinations had smaller RMS values. Differences on the order of 50 μm are important, so figure C.5 shows that the clustering algorithm had a small but notable effect. Therefore, the RMS for each tracking combination will be used to add a systematic uncertainty on the residual means.

C.4 Differential non-linearity

In this context, differential non-linearity (DNL) is when the reconstructed cluster mean is biased by the fit of the discretely sampled PDO distribution over the strips. The bias depends on the relative position of the avalanche with respect to the center of the closest strip. For a summary of DNL, refer to page 40 of Lefebvre’s thesis [31]. The cluster mean was corrected for DNL using the equation:

$$y' = y + a \sin(2\pi y_{rel}) \quad (\text{C.2})$$

where y is the cluster mean, y_{rel} is the relative position of the cluster mean with respect to the strip’s center, a is the amplitude of the correction, and y' is the corrected cluster mean.

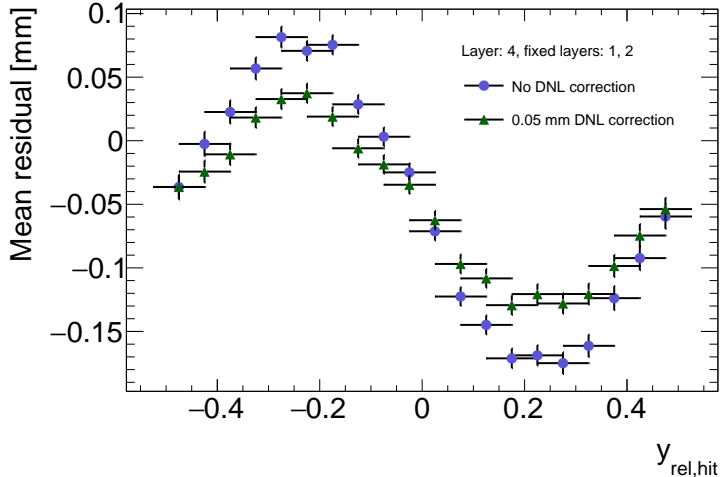


Figure C.6: Effect applying a 50 μm DNL correction to the cluster means on the residual vs y_{rel} distribution for tracks built from layers 1 and 2 and extrapolated to layer 4 for QL2.P.8.

The amplitude can be derived by comparing the reconstructed hit position to the expected hit position, as done in Abusleme, 2016 [6]. With cosmic muons, there is no reference hit position to compare to, so track residuals were used as a proxy [31]. The hallmark of the DNL effect is the periodic pattern in the residual versus y_{rel} profile, and the effect of correcting the cluster means using an amplitude of 50 μm is shown in figure C.6. An amplitude of 50 μm was based on Lefebvre's estimate of the DNL amplitudes by layer, quadruplet and cluster size using exclusive cosmic muon tracks in `tgc_analysis/CosmicsAnalysis`. Little variation was seen in the amplitude parameters with respect to the quadruplet tested, the layer and the cluster size so a universal correction was used.

Although the correction is not large enough in this case, the figure shows that the correction does reduce the DNL effect. Slightly better performance is seen in the interpolation tracking combinations where the quality of the residuals is better. DNL corrections for cosmic muon data are difficult because the DNL effect is obscured by the effect of misalignments and noise. Misalignments cause the center of the sine pattern in figure C.6 to be shifted off of zero, since the mean of residuals is shifted.

In figure C.7, it is apparent that the effect of the DNL correction on the mean of the residual distribution in 100 mm by 100 mm areas is on the order of micrometers in the worst extrapolation case. Although the σ 's of the residual distributions shrink with the DNL correction, the mean is the parameter of interest. Therefore, for this analysis DNL was not corrected for.

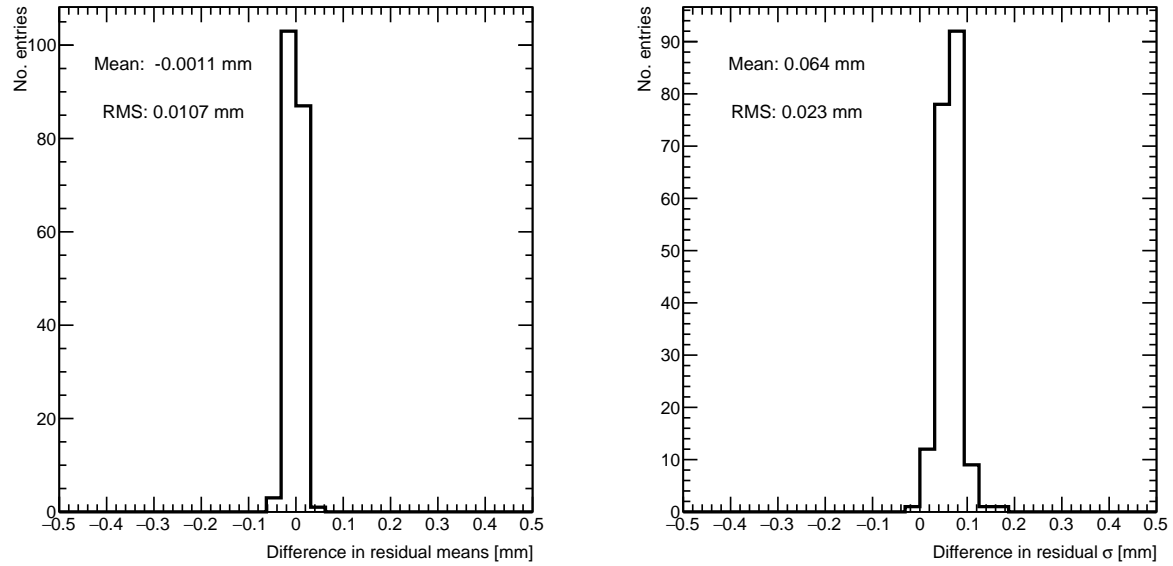


Figure C.7: Difference in residual distribution means and σ 's with and without DNL correction for residuals on layer 4 from reference layers 1 and 2 for QL2.P.8.

The σ 's of the residual distributions do shrink with the DNL correction but not so much to affect the residual means, which are the important parameter for this analysis. Therefore, since the effect of the DNL correction is negligible, it was not pursued further.

Appendix D

Printable plots

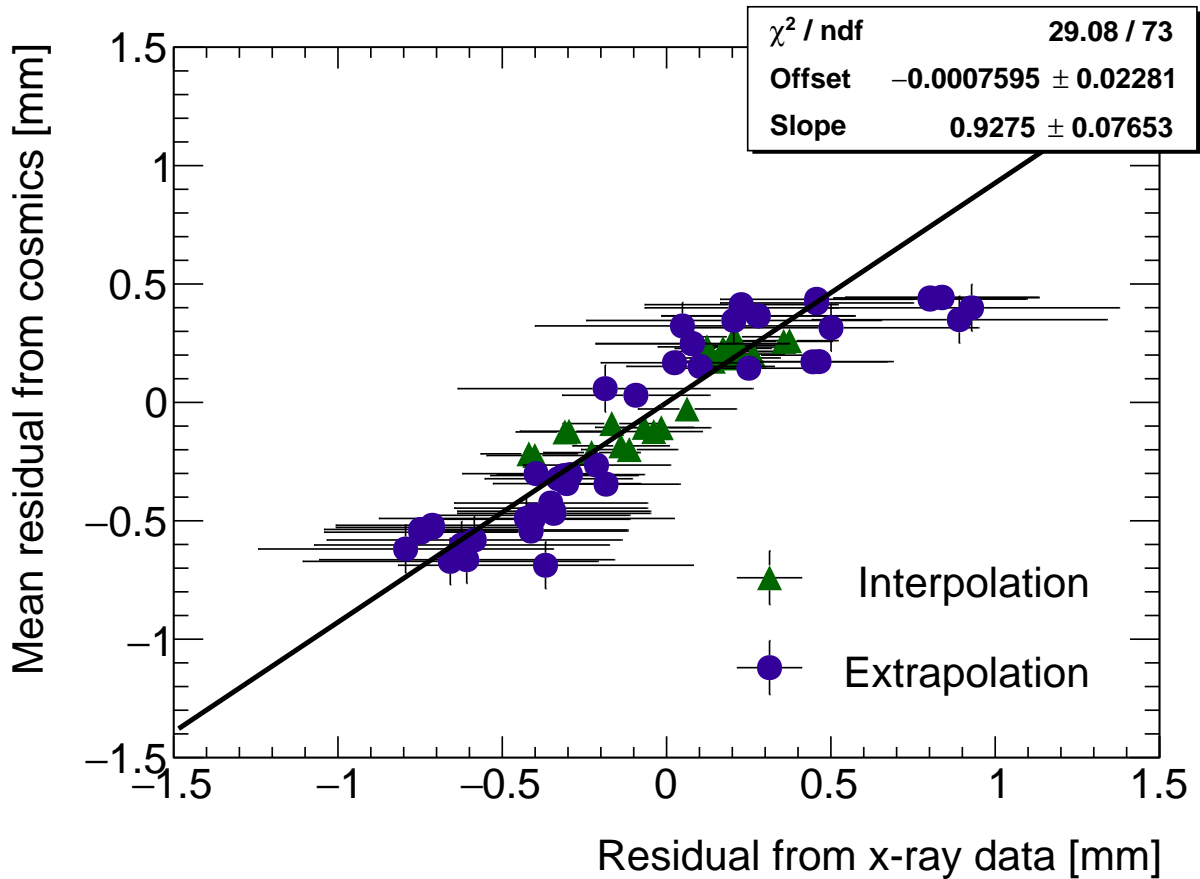


Figure D.1: Correlation plot between x-ray and cosmics residuals for all tracking combinations for QL2.P.11. Each rectangle is centered on an x-ray and mean cosmics residual pair. The width of the rectangles in x and y are the uncertainty in the x-ray and mean cosmics residual respectively. This is a printable version of figure 6.1 in section 6.2.

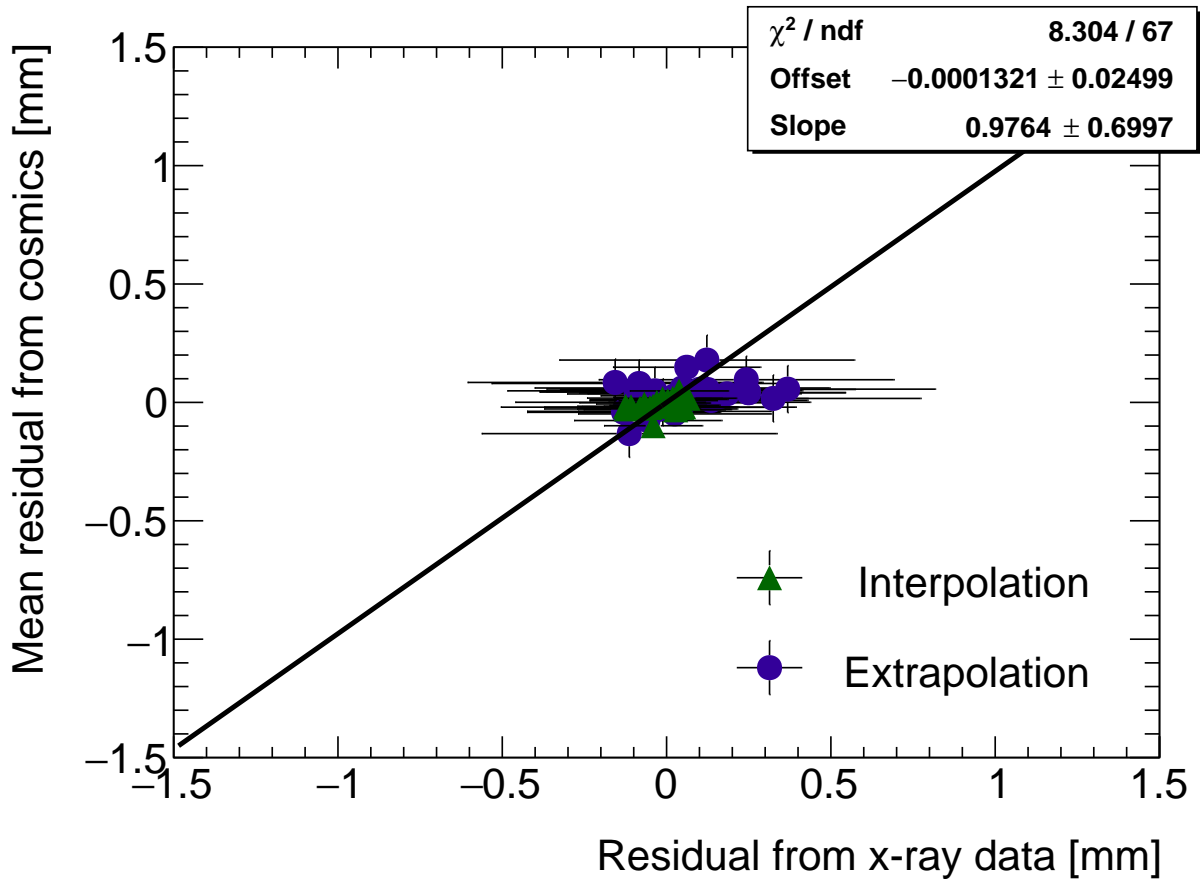


Figure D.2: Correlation plot between x-ray and cosmics residuals for all tracking combinations for QL2.P.8. Each rectangle is centered on an x-ray and mean cosmics residual pair. The width of the rectangles in x and y are the uncertainty in the x-ray and mean cosmics residual respectively. This is a printable version of figure 6.2 in section 6.2.